

SIMULATING CLUSTER FORMATION AND RADIATIVE FEEDBACK IN MOLECULAR
CLOUDS

SIMULATING CLUSTER FORMATION AND RADIATIVE FEEDBACK IN
MOLECULAR CLOUDS

By

COREY HOWARD, B.Sc.

A Thesis

Submitted to the School of Graduate Studies

in Partial Fulfilment of the Requirements

for the Degree

Master of Science

McMaster University

©Copyright by Corey Howard, September 2013

MASTER OF SCIENCE (2013)
(Physics and Astronomy)

McMaster University
Hamilton, Ontario

TITLE: Simulating Cluster Formation and Radiative Feedback in Molecular Clouds

AUTHOR: Corey Howard, B.Sc. (Queen's University)

SUPERVISOR: Ralph E. Pudritz, William E. Harris

NUMBER OF PAGES: xv, 123

Abstract

The formation of star clusters occurs in a complex environment and involve a large number of physical processes. One of the most important processes to consider is radiative feedback. The radiation released by forming stars heats the surrounding gas and suppresses the fragmentation of low mass objects. Ionizing radiation can also drive large scale outflows and disperse the surrounding gas. Owing to all this complexity, the use of numerical simulations to study cluster formation in molecular clouds has become commonplace. In order to study the effects of radiative feedback on cluster formation over larger spatial scales than previous studies, we present hydrodynamical simulations using the AMR code FLASH which make use of cluster particles. Unlike previous studies, these particles represent an entire star cluster rather than individual stars. We present a subgrid model for representing the radiative output of a star cluster which involves randomly sampling an IMF over time to populate the cluster. We show that our model is capable of reproducing the properties of observed clusters such as the luminosity, ionizing photon output, and star formation rate. The model was then incorporated into FLASH to examine the effects of radiative feedback on cluster formation in a full hydrodynamical simulation. We find that the inclusion of radiative transfer can drive large scale outflows and decreases the overall star formation efficiency by a factor of 2, consistent with previous studies. The inclusion of radiative feedback also significantly increases the degree of subclustering. The use of cluster particles in hydrodynamical simulations represents a promising method for future studies of cluster formation and the large scale effects of radiative feedback.

Acknowledgements

During my two years time working on this project, I've been fortunate enough to receive a great deal of assistance from people whose efforts I would like to acknowledge here. Firstly, I am indebted to my two supervisors, Prof. Ralph Pudritz and Prof. William Harris, who were instrumental in guiding this project. Our numerous discussions provided perspective on how my work fits into the grander scheme of astrophysics. I'd also like to thank my committee members, Prof. James Wadsley and Prof. Christine Wilson, who provided excellent insight and helped shape this work.

On the technical side, I am grateful for the help provided by the support staff of the Physics & Astronomy department at McMaster University and the SHARCNET team. In particular, I'd like to acknowledge Hua Wu (aka. the computer guru) who fixed my mistakes on multiple occasions and Sergey Maschenko who provided help with FLASH. I am also indebted to Mikhail Klassen who essentially taught me the FLASH code and was always willing to help with debugging.

And finally, I thank my family and friends for their love and encouragement. My parents have always taught me to keep an open mind and stressed the importance of education. It wasn't always been easy but Sarah was there providing the emotional support I needed and I am so grateful for that. Even though my grandmother will not be able to see this work, I sincerely hope I have made her proud and miss her with all my heart.

Only four more years until I'm forcing all of you to call me Doctor Howard!

Dedicated to my parents, Mark and Gina, without whom this thesis would not have been possible.

Table of Contents

Descriptive Notes	ii
Abstract	iii
Acknowledgements	iv
List of Figures	ix
List of Tables	xv
Chapter 1 Introduction	1
Chapter 2 Observations and theory of cluster formation and feedback	7
2.1 Star formation observations	7
2.1.1 Molecular clouds	7
2.1.2 Cluster formation and properties	9
2.1.3 The core and initial mass functions	12
2.2 Theoretical considerations	15
2.2.1 Physical Processes	15
2.2.2 Radiative transfer	20
2.2.3 Radiative feedback	23
2.2.4 Numerical simulations of cluster formation	25

Chapter 3	Cluster Particle Model	32
3.1	abstract	32
3.2	Introduction	33
3.3	Embedded star clusters: observations	37
3.4	A basic model for cluster formation	40
3.5	Results	51
3.6	Summary and Conclusions	68
Chapter 4	Numerical Methods	71
4.1	FLASH Code	71
4.2	Sink (and Cluster) Particles	72
4.3	Radiative transfer methods	74
4.3.1	Radiative transfer in FLASH	78
4.4	Heating and Ionization in FLASH	78
4.5	Adding cluster particles to raytracing	80
4.5.1	Populating the cluster with stars	80
4.5.2	Heating and ionization due to cluster particles	82
Chapter 5	Simulation Results	85

5.1	Initial conditions	85
5.2	Radiative feedback effects	86
5.3	Cluster Properties	99
5.4	The subcluster mass function	102
Chapter 6 Conclusions		108

List of Figures

1.1	The Orion Nebula as seen by the infrared WISE instrument. The image shows the filamentary structure of star forming regions. The bright source in the center, the Trapezium cluster, is a site of massive star formation. <i>Credit : NASA, JPL – Caltech, and UCLA.</i>	3
2.1	Column density map of IC 5146 obtained with SPIRE/PACS by Arzoumanian et al. (2011a). Overlaid are the 27 filaments obtained through a curvelet decomposition.	8
2.2	The SFRs in nearby star forming regions from Lada et al. (2010a). The two mass columns represent different extinction thresholds for the measurement. The left mass column represents an extinction threshold of 0.1 magnitudes while the right column is 0.8 magnitudes. . . .	10
2.3	Three proposed function forms of the IMF. The Kroupa and Muench IMFs consist of three separate powerlaws while the Chabrier IMF is a powerlaw at high masses with a lognormal turnover for stars below $1 M_{\odot}$	13
2.4	Column density plots showing the effect of external ionizing radiation (right) compared to a control run (left) from Dale et al. (2007). The incoming radiation effectively clears the gas from the forming proto-cluster.	29

3.1	Plots of the number of stars relative to the expected number versus sampling frequency for clusters with different initial masses and different constant accretion rates. The initial masses of the cluster are 100 (top left), 1000 (top right), and 10000 (bottom left) M_{\odot} . The solid lines represent stars less than 1 M_{\odot} and dotted lines represent stars greater than 1 M_{\odot}	41
3.2	A subset of our data showing the luminosity, number of ionizing photons, and the star formation rate. Blue, red, and green lines represent accretion rates of 0, 2.8×10^{-3} and $2.8 \times 10^{-2} M_{\odot} \text{ yr}^{-1}$, respectively. The columns, from left to right, represent initial clump masses of 100, 1000, and 10000 M_{\odot}	43
3.3	The total gas mass, the mass in stars, and the reservoir mass as a function of time for an initial clump mass of 1000 M_{\odot} . The panels from left to right represent models with an accretion rate of 0, $2.8 \times 10^{-3} M_{\odot} \text{ yr}^{-1}$, and $2.8 \times 10^{-2} M_{\odot} \text{ yr}^{-1}$	45
3.4	The resulting mass function for models with no accretion (left) and an accretion rate of $2.8 \times 10^{-2} M_{\odot} \text{ yr}^{-1}$ (right) for initial clump masses of 100 (top), 1000 (middle), and 10000 (bottom) M_{\odot} . The red circles represent the normalized Chabrier IMF.	49

3.5 The resulting mass function for models with the same final clump mass but have either accreted all the mass (left) or had no accretion and the mass was present initially (right). From top to bottom, the final clump masses are 500, 5000, and 50000 M_{\odot} . The red circles represent the normalized Chabrier IMF. 50

3.6 The total number of stars, the number of O stars, and the final luminosity of runs with varying accretion rates and initial clump masses. The points represent the average of all runs and the error bars represent one standard deviation. 53

3.7 A reference figure showing the final clump masses for the models run in Figure 3.6 with the same colour coding. The dotted black line shows separates the accretion and reservoir dominated regimes. 58

3.8 The instantaneous SFR as a function of total clump mass at 2 freefall times. Error bars represent the resulting standard deviations from 100 identical runs. The α parameters shown in the plots are the resulting indexes from powerlaw fits to the data. The error on α , obtained through the fitting, is also shown. 61

3.9 The SFR versus clump mass for this work, shown in blue, and observations presented in Lada et al. (2010a), shown in black. The observed SFRs are systematically lower compared to our model. 64

3.10	The percentage of O stars formed from the models shown in Figure 3.6. As discussed in the text, the expected percentage of O star from directly integrating the IMF is 0.28%. The points represent the average of all runs and the error bars represent one standard deviation. The colour coding is the same as in Figure 3.6.	67
4.1	A comparison between long characteristics (left) and short characteristics (right) raytracing from Rijkhorst et al. (2006). In the long characteristics method, a ray is drawn from the source to all cells resulting in redundant calculations shown by multiple rays passing through the same cells. The short characteristics method avoids this redundancy but is inherently serial.	77
5.1	A density slice (in g cm^{-3}) showing a slice through the center of the z-axis for run RHD6. The locations of the cluster particles are projected onto this slice and shown by the black dots. The plots represent times of 0.15, 0.5, 0.75, and 1 Myrs from top to bottom and left to right. . .	90
5.2	A density slice (in g cm^{-3}) showing a slice through the center of the z-axis for run HD6. The locations of the cluster particles are projected onto this slice and shown by the black dots. The plots represent times of 0.15, 0.5, 0.75, and 1 Myrs from top to bottom and left to right. . . .	91

5.3 Density slices (in g cm^{-3}) along the z-axis showing the emergence of a large number of cluster particles in RHD6. Interactions between cluster particles produces an overdense region which rapidly fragments to form new particles. The plots are shown at times of 0.93, 0.95, 0.97. and 0.99 Myrs. 92

5.4 Temperature slices (in Kelvins) through the x-axis showing a side on view of an outflow emerging from a group of particles clustered near the center of the computational volume in RHD6. The arrows show the velocity of the gas, indicating that the loop structure is indeed an outflow. 93

5.5 The density corresponding to the plots shown in Figure 5.4. The outflow is is launched into a region of low density and is confined by a filament on one side. 94

5.6	Top: A plot showing the mass of all cluster particles that form in the three simulations as a function of time. RHD6, HD6, and HD8 are coloured red, blue, and black, respectively. Lines that end abruptly are either due to the simulation ending or merger events. Bottom: The total mass present in cluster particles as a function of time and the respective star formation efficiency. The total mass in clusters is given by the solid lines and the star formation efficiency by the dashed lines. Note that the star formation efficiency is defined as the total mass in clusters divided by the instantaneous mass in the simulation to account for mass growth. Clearly, radiative feedback is strongly suppressing the formation of clusters.	96
5.7	The accretion rates as a function of time for the two most massive particles in RHD6 (top) and HD6 (bottom).	99
5.8	Top: The SFR as a function of time for the three most massive particles in run RHD6. Bottom: The luminosity evolution of the three most massive particles in RHD6 (shown by the dashed lines) and the total luminosity of all particles (solid line). The total luminosity is dominated by one single particle whose track is drawn but cannot be seen because it is covered by the total luminosity line.	101
5.9	The ECMF for run RHD6 shown at three different times. The largest mass particles form first followed by the burst of smaller mass particles which fill out the lower mass end of the ECMF.	105

List of Tables

5.1	Summary of simulation parameters and results	86
-----	--	----

Chapter 1

Introduction

The formation, evolution, and death of stars involves a vast range of physical processes that take place inside our universe. The formation of stars is directly coupled with planet formation which is a prerequisite for life. The evolution of stars, and their subsequent deaths, drive the large-scale evolution of galaxies. Moreover, almost every element other than hydrogen and helium has been synthesized in the cores of stars through nuclear fusion. These few examples illustrate why the study of stars has been at the center of astronomy and astrophysics since its advent.

The formation of stars in the Milky Way takes place in large collections of cold molecular gas known as giant molecular clouds (GMCs). GMCs have typical sizes of 40-100 pc, temperatures of 10-20 K, and total masses from 10^5 to $10^7 M_{\odot}$ (Fukui & Kawamura, 2010). The conversion of this molecular gas into fully formed stars involves a wide variety of physical processes. Gravity is the most important mechanism in the star forming process. Small density fluctuations in the cloud can lead to fragmentation which refers to small regions of the cloud undergoing rapid runaway collapse.

Stars do not fragment out of their parent cloud in isolation. Overdense regions in the molecular cloud, known as clumps, are home to many sites of star formation resulting in a star cluster. The variation between star clusters is immense. They can range from small clusters containing tens of stars, such as Serpens South (Kirk et al., 2013), to clusters like R136 which contains thousands of stars with over 120 of those being OB stars (Massey & Hunter, 1998). Moreover, it is estimated that $\sim 90\%$ of stars form in a clustered environment which means that understanding the details of cluster formation is crucial to a complete understanding of star formation.

While there is a large amount of variation between the properties of star clusters, there is little to no variation in their stellar content (Chabrier, 2005). The initial mass function (IMF) represents the distribution of stellar birth masses from one collective star forming event. While there are different competing forms for the IMF, there appears to be no variation of the IMF between star forming regions (Chabrier, 2005). This applies for both galactic and extragalactic sources. It is therefore important to isolate and understand the processes that are responsible for the IMF.

Recent advances in far infrared imaging, especially through the use of *Herschel*, have revealed the complexity of star forming environments. Molecular clouds are filled with filaments which are hosts to star formation. This is especially true for regions where filaments intersect. The filamentary nature of molecular clouds has been attributed to supersonic turbulence which is generated through repeated shocking of the gas (Pudritz & Kevlahan, 2012). Not only is turbulence responsible for generating the architecture of the star forming environment, but it is also thought to



Figure 1.1: The Orion Nebula as seen by the infrared WISE instrument. The image shows the filamentary structure of star forming regions. The bright source in the center, the Trapezium cluster, is a site of massive star formation. *Credit : NASA, JPL – Caltech, and UCLA.*

be responsible for the broad features of the IMF (Padoan & Nordlund, 2005; Clark & Klessen, 2008).

Radiative feedback, like turbulence, is another process which can affect the features of the IMF. The formation of stars is an energetic process. The gravitational collapse of a star forming core, its subsequent accretion, and the ignition of nuclear burning releases a significant amount of energy as radiation. Absorption of infrared radiation causes the dust and gas surrounding the star forming region to increase in temperature. This has been shown to alter the fragmentation properties of the gas, namely to suppress the fragmentation of low mass objects. The release of UV radiation also ionizes the surrounding molecular gas. This results in large parsec-scale bubbles of hot ionized gas known as HII regions. The expansion of an HII region can clear out gas from a cluster forming region and completely halt the accretion process. Such processes can ultimately lead to the dispersal of the GMC (?).

The use of numerical simulations has allowed the study of how these complex and interconnected processes shape star formation. While significant progress has been made in studying the role of individual processes, several challenges remain. Firstly, a full hydrodynamical simulation which contains all relevant physical processes is yet to be completed due to computational constraints. Secondly, it is not currently feasible to study the collapse of an entire molecular cloud down to individual stellar densities. Instead, a computational tool called sink particles is used to replace regions of high density gas which are collapsing to form an individual protostar. This technique has its limitations, however. Large molecular clouds can form thousands of stars or more and following the formation and dynamical interactions between these particles is

computationally expensive. This is especially true when the particles are coupled to a radiative transfer scheme. Studies are therefore limited to studying small subregions of molecular clouds and, even then, are not evolved long enough to fully disperse the surrounding gas.

In this work, we attempt to study the formation of star clusters, and the effect that their formation has on their surroundings, over the scale of an entire molecular cloud through the use of cluster sink particles. These particles work with the same principle as sink particles used to represent stars but instead represent an entire stellar cluster. We have coupled our cluster sink particles with a raytracing method to treat radiative transfer, similar in principle to Harper-Clark (2011). This has several advantages. Since we are not resolving down to individual stars, we are able to study the formation of clusters over an entire molecular cloud rather than just a subregion. This allows us to study how the formation of a cluster can alter its surroundings via radiative feedback on its natal cloud, possibly altering the formation of clusters in other regions of the cloud. The decreased number of particles that need to be considered also allows us to evolve our simulation for much longer compared to those using stellar sink particles.

In order to couple our particles with a radiative transfer scheme, a subgrid model is needed to represent the radiative output of an entire star cluster. The details of this model are described in Chapter 3 and compared against observation to confirm its validity. The implementation of this model into the hydrodynamical code FLASH and details of the radiative transfer scheme, known as raytracing, are then discussed in Chapter 4. Chapter 5 is dedicated to the results of three hydrodynamical sim-

ulations which examine the effects of radiative feedback on cluster formation. The overall aim of this work is to construct a more complete picture, which is consistent with recent observations, of how radiative feedback from forming clusters affects its formation and the role this plays in dispersing progenitor molecular clouds.

Chapter 2

Observations and theory of cluster formation and feedback

2.1 Star formation observations

2.1.1 Molecular clouds Stars are born within large collections of molecular gas called Giant Molecular Clouds (GMCs). GMCs from different galaxies show similar properties; typical sizes are 40-100 pc with masses between 10^5 to $10^7 M_{\odot}$ (Fukui & Kawamura, 2010). The star formation activity within a cloud is intimately related to its physical properties and structure. For example, the star formation rate, defined as the total mass converted to stars per year, within a molecular cloud scales linearly with its dense gas mass (Wu et al., 2005; Gao & Solomon, 2004; Lada et al., 2010b). This is a robust result which holds for both galactic and extragalactic clouds regardless of the molecular tracers used to measure the star formation rate.

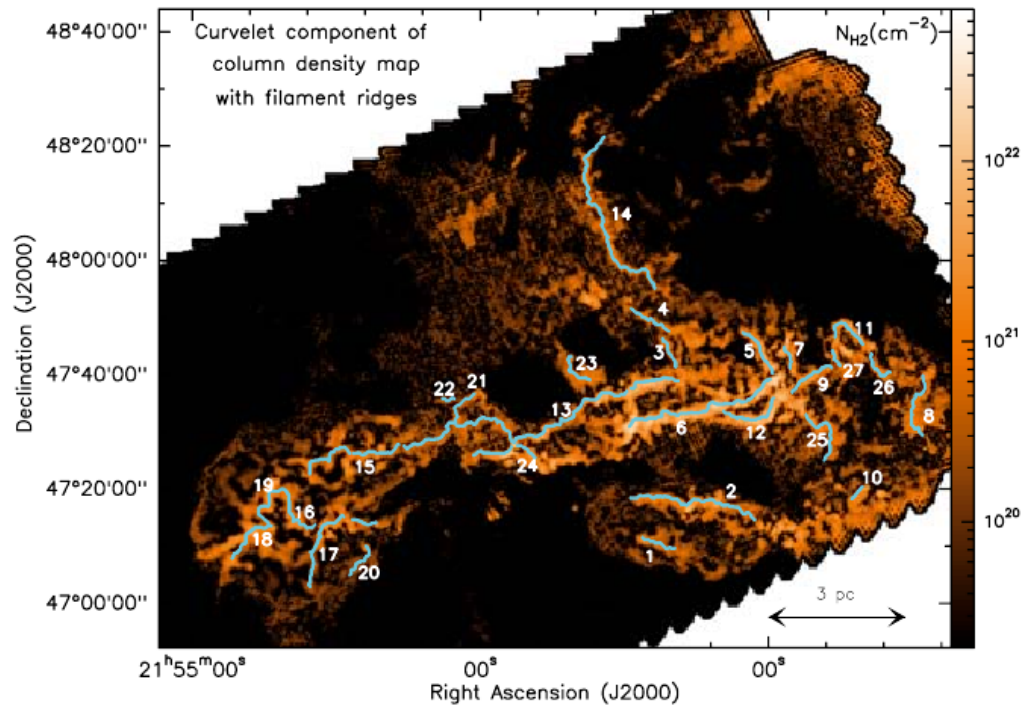


Figure 2.1: Column density map of IC 5146 obtained with SPIRE/PACS by Arzoumanian et al. (2011a). Overlaid are the 27 filaments obtained through a curvelet decomposition.

Recent far-infrared studies with *Herschel* are revealing the complicated internal structure in molecular clouds. Namely, clouds are found to be far more filamentary than early surveys suggested (André et al., 2011; Schneider et al., 2012). This network of dense, parsec-scale long filaments is likely due to intersecting, turbulent shocks in the gas due to a variety of sources such as expanding HII regions, stellar winds, and supernovae (Pudritz & Kevlahan, 2012). Observations suggest that these high density filaments are also the sites of star formation (Hill et al., 2011a; Arzoumanian et al., 2011b) which highlights the importance that turbulence plays in the star formation process. The largest areas of star formation occur at the intersection of filaments as observed in the Rosette molecular cloud (Hill et al., 2011b; Schneider et al., 2012). The forming cluster is then fed with accretion flows flowing along the filament, perhaps extending the star formation timescale (Kirk et al., 2013).

2.1.2 Cluster formation and properties Star clusters are broadly defined by Lada & Lada (2003) as physically correlated stellar systems which contain a high enough stellar density to be stable, if the cluster was in virial equilibrium, against tidal disruption. To be considered a cluster, the grouping of stars must also have an evaporation time (ie. the time it takes for a cluster to dissolve via dynamical interactions and ejections) which is greater than 100 Myrs since this is the observed lifetime of open clusters. These conditions roughly translate to groupings which have greater than 35 stars and a stellar volume density which exceeds $1 M_{\odot} \text{ pc}^{-3}$ (Lada & Lada, 2003).

Cloud	Mass (M_{\odot}) ^a	Mass (M_{\odot}) ^b	No. of YSOs	References	SFR($10^{-6} M_{\odot}\text{yr}^{-1}$)
Orion A	67,714	13,721	2862	1,2,3	715
Orion B	71,828	7261	635	4,5	159
California	99,930	3199	279	6,7	70
Perseus	18,438	1880	598	8,9,10	150
Taurus	14,964	1766	335	11	84
Ophiuchus	14,165	1296	316	12	79
RCrA	1,137	258	100	13,14, 15	25
Pipe	7,937 ^c	178	21	16	5
Lupus 3	2,157	163	69	17, 18,	17
Lupus 4	1,379	124	12	17, 18,	3
Lupus 1	787	75	13	17, 18,	3

Figure 2.2: The SFRs in nearby star forming regions from Lada et al. (2010a). The two mass columns represent different extinction thresholds for the measurement. The left mass column represents an extinction threshold of 0.1 magnitudes while the right column is 0.8 magnitudes.

Clusters are estimated to be formed at a rate of $2\text{-}4 \text{ Myrs}^{-1} \text{ Kpc}^{-2}$ in the solar neighbourhood (Lada & Lada, 2003). Since the vast majority of stars ($\sim 90\%$) form in clustered environments, understanding their formation, structure, and evolution is crucial to a complete theory of star formation.

The formation of clusters takes place inside clumps which are overdense regions in molecular clouds which may or may not be gravitationally bound. Clumps have typical densities, in the Milky Way, of $10^2\text{-}10^4 \text{ cm}^{-3}$, sizes of $0.04\text{-}1 \text{ pc}$, and masses of $0.1\text{-}10^3 M_{\odot}$ (Veltchev et al., 2013). The transition between starless and star-forming clumps occurs at a density of roughly 10^4 cm^{-3} (Lada & Lada, 2003). Clumps then fragment into smaller collapsing regions known as cores which form individual stars or multi-star systems (binaries, triples, etc.) (?).

The early evolution of cluster formation is difficult to observe in the optical regime due to dust obscuration, but recent advances in far-IR imaging have made embedded cluster observations possible. An important observational result is the embedded

cluster mass function. This function represents the number of embedded clusters with a total stellar mass content between masses m and $m + dm$. Surveys have revealed that, down to the observational limit, the embedded cluster mass function can be represented as,

$$dN \propto m^{-2}dm \quad (2.1)$$

where m is the cluster mass, and N is the number of clusters between m and $m + dm$ (Fall & Zhang, 2001; Bik et al., 2003; Lada & Lada, 2003).

The morphology of embedded clusters provides some important evidence about their formation. Embedded clusters are not observed to be spherical but elongated with an aspect ratio of approximately 2 (Lada, 2010). Lada & Lada (2003) have shown that there are generally two types of embedded clusters; clusters which are compact and centrally condensed, and those that exhibit irregular surface density structures with multiple peaks. The irregular surface densities are evidence for subclustering which can be washed out through dynamical interactions as the cluster evolves.

Subclustering has been observed in the early stages of cluster formation for a variety of star forming regions of different masses (Testi et al., 2000; Yan et al., 2010; Gouliermis et al., 2012). These all show that clusters are not born as large, centrally condensed objects but are instead built up of smaller clustered regions whose stellar densities are significantly higher than the average. The ages of these subclusters are not necessarily the same and can differ by a million years or more. It is estimated

that these regions will merge through dynamical interactions in approximately three million years.

There is also evidence that the separations between stars are not what would be expected from a random distribution, but instead strongly peaked (Teixeira et al., 2006). The peak separation corresponds to the Jeans length of the star forming region.

The star formation rates (SFRs) in embedded clusters vary dramatically between regions. Figure 2.2 shows the SFRs in nearby star forming regions. The large variation in SFRs is due to the availability of dense, star-forming gas. It has been conclusively shown that the SFR and the number of forming protostars scales linearly with the amount of dense gas in the region (Wu et al., 2005; Gao & Solomon, 2004; Lada et al., 2010b).

Clusters do not remain embedded indefinitely as the gas is eventually cleared from the region through stellar feedback. The majority of embedded clusters do not survive the emergence; $\sim 90\%$ of clusters dissolve within 10 Myrs due to internal dynamical interactions (Lada & Lada, 2003).

2.1.3 The core and initial mass functions The fragmentation of clumps and filaments gives rise to the formation of cores which are the early stage progenitors of main sequence stars. Widefield sub-mm observations with cameras such as SCUBA and MAMBO have allowed the identification of numerous of these cold and compact cores which are intermediates between diffuse CO clumps and young stellar objects

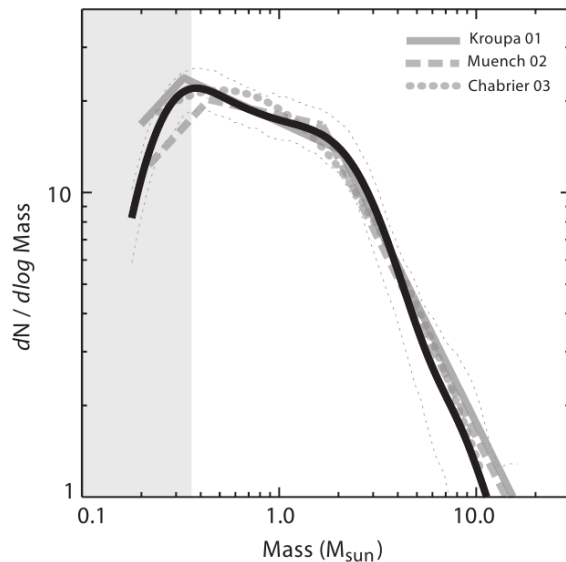


Figure 2.3: Three proposed function forms of the IMF. The Kroupa and Muench IMFs consist of three separate powerlaws while the Chabrier IMF is a powerlaw at high masses with a lognormal turnover for stars below $1 M_{\odot}$.

(Johnstone et al., 2001; Motte et al., 2001; Nutter & Ward-Thompson, 2007; Enoch et al., 2008). An important result from these studies is the core mass function (CMF) which is represented as dN/dM , where m represents the core mass and N is the number of cores having masses between m and $m + dm$. The mean core mass in regions such as ρ Ophiuchi and Orion is $\sim 0.2-1.5 M_{\odot}$ (André et al., 2011) and the form of the CMF is well-fit with a lognormal distribution with a high mass powerlaw tail (see Chabrier (2009) for a discussion on the form of the CMF).

The initial mass function (IMF) is the mass spectrum of stars born collectively in one star forming event and is represented in the same way as the CMF except in this case m represents stellar mass and N is the number of stars having masses

between m and $m + dm$. Being able to reproduce the observed IMF is a necessity for a complete theory of star formation.

The first work on the IMF by Salpeter (1955) found that the high mass end of the IMF can be expressed as $\xi(m) \propto m^{-1.35}$. However, significant progress has been made on the function form of the IMF since its introduction through a variety of observational techniques. The first step in measuring the IMF is to determine the luminosity function of the region of interest (Kroupa et al., 2013). The luminosity function is analogous to the mass function but represents the number of stars at a given magnitude. Once the luminosity function is known, the mass function can be determined through the use of a mass-luminosity relation for stars which is obtained through detailed stellar structure modeling. This method (Kroupa et al., 2013) has been applied to galactic field stars and stellar clusters (which have the advantage of being an equidistant and co-eval sample of stars).

While different functional forms of the IMF have been fit to the results of these surveys (see Figure 2.3 for some examples), there are several general conclusions that can be drawn. The first is that the Salpeter slope is accurate for stars above $1 M_{\odot}$ (Alves et al., 2007). Below $1 M_{\odot}$, there is a turnover indicating that very low mass stars are less prevalent. One form of the IMF proposed by Chabrier (2005), and the one used throughout this work, fits the lower mass end of the IMF with a lognormal distribution and a high mass powerlaw tail,

$$\xi(\log m) = \begin{cases} 0.093 \times \exp\left\{\frac{-(\log m - \log 0.2)^2}{2 \times (0.55)^2}\right\}, & m \leq 1 \text{ } M_{\odot} \\ 0.041m^{-1.35 \pm 0.3}, & m > 1 \text{ } M_{\odot}. \end{cases} \quad (2.2)$$

Surveys also suggest that the IMF is universal to within current observational limits (?). This holds true for both galactic and extragalactic stars regardless of the star-forming environment suggesting that star formation is a self-regulating process.

2.2 Theoretical considerations

2.2.1 Physical Processes

Recent theoretical and numerical studies have revealed that star formation involves significantly more physical processes than initially included in early analytical models. The interplay between gravity and turbulence is an especially important topic (see review by Ballesteros-Paredes et al. (2007)). As mentioned earlier, repeated shocking of the gas is responsible for the filamentary star forming environment observed in molecular clouds. Turbulent motions within molecular clouds are also responsible for the observed lognormal column density probability function (PDF) (Vázquez-Semadeni et al., 2006; Kevlahan & Pudritz, 2009). It has been proposed that this lognormal PDF could be partly responsible for the form of the IMF, especially at the low mass end (Padoan & Nordlund, 2002a).

Gravity is connected to turbulence through the gravitational collapse of the high density fluctuations which determine the core mass function. Observations of the core mass function reveal that it has the same form as the IMF except shifted upwards in mass by approximately a factor of 3 (Goodwin et al., 2008; Chabrier & Hennebelle, 2010). This provides an estimate of the star formation efficiency since roughly two-thirds of the gas is dispersed in the transition between a core and a fully formed star.

The similarity between the IMF and the CMF also provides further evidence about how cluster formation occurs. There have been two theories proposed for the formation of stars in a cluster; competitive accretion and turbulent fragmentation.

Competitive accretion posits that stellar seeds form at a mass of roughly $0.1 M_{\odot}$ and subsequently accrete the required gas to form a protostar (Bonnell, 2005). This mechanism assumes that the gas is not bound on scales smaller than a clump, so the problem can be treated as non self-gravitating gas accreting onto point particles. This is known as Bondi-Hoyle accretion and leads to the accretion rate varying as $\dot{m} \propto m^2$ (Krumholz et al., 2006a). Therefore, as the stellar seed grows in mass, the accretion rate also grows. In a clustered environment, several of these seeds will be accreting and will be competing for the available gas in the clump. This mechanism provides an explanation for the mass segregation seen in clusters; the first seeds to form in the local gravitational minimum will accrete the most gas and so the highest mass stars will be preferentially found in the center of the cluster (Krumholz et al., 2005).

While early simulations found that competitive accretion can result in the observed IMF, more recent works have pointed out flaws. The first is that it assumes clumps are not gravitationally bound which is not consistent with observations (Krumholz et al., 2005). Secondly, if stars get the majority of their mass through accretion then there should be a large difference between the masses of protostars still in the accretion phase compared to fully formed galactic field stars. This difference is also not observed (Krumholz et al., 2005). Competitive accretion also posits that cores and the surrounding gas should have significantly different velocities but this difference is also not observed (Kirk et al., 2007).

The fact that the CMF is shifted to higher mass by a factor of 3 compared to the IMF suggests that the second mechanism, turbulent fragmentation, is the more likely mechanism for star formation. This is a “top-down” approach meaning that prestellar cores fragment out of the parent clump via the dissipation of supersonic turbulence and are not built up through accretion alone. The transition between the CMF and the IMF is then due to the effects of stellar feedback which disrupt the gas in the star-forming cores. Theoretical modeling (Matzner & McKee, 2000; Fall et al., 2010) which includes the effects of feedback into a turbulent fragmentation scenario have found a star formation efficiency of $\sim 30\%$, consistent with observations of the offset between the CMF and the IMF. Moreover, numerical simulations of turbulent fragmentation are able to reproduce the Salpeter slope (Padoan & Nordlund, 2002b, 2005).

There are some caveats to turbulent fragmentation and the origin of the IMF. First, it assumes a one-to-one mapping between cores and protostars which ignores

the formation of binaries or multiple systems. Clark et al. (2007) have pointed out that this assumption leads to star formation timescale inconsistencies which require the CMF and the IMF to have different forms. The resulting mass functions also depend heavily on the way the interstellar turbulence is driven. Large-scale driving of the turbulence results in a mass spectrum that resembles the IMF (Clark & Klessen, 2008). However, if turbulence is introduced on smaller spatial scales the cores are built up independently and are more easily disrupted, resulting in inefficient star formation (Klessen et al., 2000). It is clear that a full understanding of the stellar IMF requires more physical processes than just turbulence and gravity.

Stellar feedback, which occurs in many forms, is responsible for slowing the growth of protostars and eventually stopping the star formation process entirely. The following is a list of relevant feedback mechanisms accompanied by a brief description;

- **Radiative feedback:** Heating and ionizing radiation, mostly from OB stars, changes the local properties of the star forming gas (Offner et al., 2009; Dale et al., 2007; Hansen et al., 2012; Dale et al., 2012). This process is described in more detail in the next section.
- **Radiation pressure:** Photons released from a forming protostar scatter off gas/dust and transfer momentum to the surrounding material. This form of feedback is especially important in simulations of high mass star formation where early results found that it is sufficient to stop the accretion process al-

together (Cunningham et al., 2011; Kuiper et al., 2010).

- **Supernovae feedback:** Massive stars evolve to the main sequence significantly faster than their low mass counterparts and explode as supernovae. The resulting release of energy is sufficient to clear the gas completely from the star forming region (Hensler, 2011).
- **Jets, winds, and outflows:** High temperatures and magnetic fields drive the release of both neutral and charged particles from the stellar surface in the form of a wind which interacts with infalling gas. Magnetic fields twisted up in the protostellar disk drive outflows perpendicular to the disk (unlike stellar winds which are more spherically symmetric). The resulting jets affect the accretion flow onto the forming protostar but are probably not responsible for the large scale clearing of gas from the cluster (see review by Pudritz et al. (2007)).

Like the above processes, the presence of magnetic fields also slows the star formation process by providing a large-scale pressure support of low density gas against gravitational collapse (Myers & Goodman, 1988). On smaller scales, some simulations show that the support due to magnetic fields is strong enough to prevent the formation of a protostellar disk (Mellon & Li, 2008; Hennebelle & Fromang, 2008) altogether. Seifried et al. (2013) showed that this problem can be avoided by the

inclusion of turbulence indicating the above processes do not exist in isolation and must be considered together to have a full understanding of star formation.

2.2.2 Radiative transfer

The transmission of radiation through a medium is a problem which arises throughout many areas of astrophysics. It is a difficult problem to solve fully, however, due to the overwhelming numerical complexity.

In the absence of scattering and in one dimension, we can represent the specific intensity (or brightness) of a beam of light as it travels through a medium via the radiative transfer equation which is given by,

$$\frac{dI_\nu}{ds} = -\alpha_\nu I_\nu + j_\nu \quad (2.3)$$

where I_ν is the intensity of the beam with frequency ν , ds is a differential path length, α_ν is the absorption coefficient in units of inverse length, and j_ν is the emission coefficient. This is a simplified treatment which only considers absorption along the path of the beam (represented by the first term on the right hand side of the above equation) and emission (second term on right hand side) in one dimension with no scattering into the beam.

Solving the above equation is simplified when considering absorption or emission only. In the case of absorption only, the beam intensity is given by,

$$I_\nu(s) = I_\nu(s_0) \exp\left[-\int_{s_0}^s \alpha_\nu(s') ds'\right] \quad (2.4)$$

indicating that the brightness of the beam decreases by the exponential of the absorption coefficient integrated along the line of sight.

The beam intensity in the opposite case (ie. emission only) is given by,

$$I_\nu(s) = I_\nu(s_0) + \int_{s_0}^s j_\nu(s') ds' \quad (2.5)$$

meaning the increase to the brightness due to emission is equal to the emission coefficient integrated along the line of sight.

The radiative transfer equation is typically expressed not in terms of physical distances, s , but by the optical depth, τ_ν , given by

$$\tau_\nu(s) = \int_{s_0}^s \alpha_\nu(s') ds'. \quad (2.6)$$

A region is said to be optically thick (or opaque) if $\tau_\nu > 1$ meaning that a typical photon of frequency ν cannot traverse a medium without being absorbed. On the other hand, if $\tau_\nu < 1$ then the region is optically thin and a typical photon can pass through the medium without being absorbed. Using optical depth, the radiative transfer equation takes the following form

$$\frac{dI_\nu}{ds} = -I_\nu + S_\nu \quad (2.7)$$

where S_ν is called the source function and is defined as the ratio between the emission and absorption coefficient.

The material properties of the medium enter through the opacity coefficient, $\kappa_\nu(\text{cm}^2 \text{g}^{-1})$, which is related to the absorption coefficient through,

$$\alpha_\nu = \rho\kappa_\nu \quad (2.8)$$

where ρ is the mass density. In most astrophysical situation, the largest contributor to the opacity is dust grains. At specific frequencies, line absorption by certain molecular species can also contribute to the opacity. The frequency dependence of the opacity complicates the radiative transfer equation. Many numerical simulations involving radiative transfer use a single-valued opacity which is a frequency average of the frequency dependent opacity; the 'grey-atmosphere' approximation. This approximation, however, has its disadvantages. Since a single value of opacity is assumed, the absorption in the infrared is typically overestimated since the the gas is more transparent to radiation in comparison to UV wavelengths where absorption is underestimated due to increased opacity. A multi-wavelength approach to radiative transfer is more accurate but difficult to implement efficiently.

In the context of star formation simulations, radiative transfer plays an important role. The immediate area surrounding the collapsing prestellar region is optically

thick (including the protostellar disk) so radiation is absorbed and re-emitted by dust at lower frequencies. Regions can become optically thin after gas has been cleared meaning that radiation can travel long distances before interacting with the medium. The effects of radiation on the star formation process is described in more detail below and numerical methods to treat radiative transfer are described in Chapter 4.

2.2.3 Radiative feedback The star formation process releases energy in the form of heat and ionizing radiation which has a significant impact on the local gas properties (Price & Bate, 2009; Krumholz et al., 2010). The fragmentation and gravitational collapse of cores in a site of active star formation is suppressed due to the increased temperature. This can be understood in terms of changes in the Jeans length. The Jeans length is the critical size scale for a spherical core below which hydrostatic pressure support is not sufficient to prevent gravitational collapse and is given by,

$$\lambda_J = \sqrt{\frac{15k_B T}{4\pi G \mu \rho}} \quad (2.9)$$

where k_B is Boltzmann's constant, T is the temperature, μ is the mean molecular weight, and ρ is the density. It can be seen that as the temperature increases, the Jeans length also increases meaning that local density fluctuations do not as easily trigger collapse. Ionization of the gas also acts to increase the Jeans length since an increased ionization fraction corresponds to a decreased mean molecular weight.

Including ionization routines in radiative feedback codes is vital to reproduce observations. Large regions of low density, hot ($\sim 5000\text{-}20000$ K), partially ionized gas known as HII regions are observed to surround locations of recent star formation (Mezger & Henderson, 1967; Shields, 1990). These regions are produced by the ionizing radiation released from massive stars as evidenced by smaller ultra-compact HII regions which surround massive stars that are still deeply embedded in their natal clouds (Churchwell, 2002). Expanding HII regions may also be responsible for triggered star formation via the collect and collapse process (Dirienzo et al., 2012; Zavagno et al., 2010) in which the expanding front collects enough material to become gravitationally unstable and form stars.

The interaction of radiation with a surface through scattering and absorption also induces a pressure on the material which can be related to the energy density, u , through

$$P = \frac{u}{3}. \quad (2.10)$$

In the context of star formation, UV and optical radiation is absorbed by dust grains and re-emitted in the infrared. Since dust grains are coupled to the surrounding gas through collisions, a pressure is exerted on both the gas and the dust. Radiation pressure is especially important in studies of massive star formation. Until recently, it was debated how massive stars form because in numerical simulations the radiation pressure was so effective in stopping the accretion flow the protostars could not grow above approximately $40 M_{\odot}$ (Kuiper et al., 2012). Only through the

introduction of more accurate radiative transfer schemes has the issue been resolved (Kuiper et al., 2012).

It is clear that including radiative transfer into hydrodynamical simulations of star formation is vital for reproducing observations and for understanding how heating, radiation pressure, and ionization affect fragmentation. We have this capability in FLASH, which is used in this work, through the use of a raytracing scheme that is described in Chapter 4.

2.2.4 Numerical simulations of cluster formation

Hydrodynamical simulations of cluster formation have only become possible over the past couple of decades due to advances in computational resources. There are two computational techniques used in these simulations to solve the fluid equations; Adaptive Mesh Refinement (AMR), and Smoothed-particle Hydrodynamics (SPH). AMR solves the fluid equations on a Eulerian mesh which selectively increases the resolution in regions of interest. AMR has the advantage of being able to treat fluid discontinuities accurately but does not exactly conserve angular momentum and is difficult to implement. SPH, on the other hand, is a purely Lagrangian code and works by discretizing the fluid into distinct particles whose properties are later 'smoothed' over an effective length to obtain relevant physical parameters. While SPH does conserve angular momentum and automatically gets higher resolution in dense regions, it suffers from the treatment of fluid discontinuities. This work will focus on AMR since the code we use, FLASH, falls into this category.

Even though significant progress has been made in simulations of cluster formation, it still suffers from some fundamental limitations. The main issue is that following the collapse of a diffuse collection of gas down to individual stellar densities is not currently possible (Federrath et al., 2010). As a result, the use of sink particles has become ubiquitous. The gas that exceeds a certain density threshold, among other criteria, is replaced by a particle of equal mass which is able to accrete gas and interact gravitationally with its surroundings. Any physics occurring on scales smaller than the sink particle is not resolved so subgrid models must be implemented. Sink particles are typically used to represent a single star or, more accurately, a dense and bound collection of gas which will soon become a star.

Early simulations of star formation suffered from artificial fragmentation, meaning that the perturbations that arise from the discretization of the hydrodynamical equations can lead to the formation of artificial fragments, which are overdense regions that undergo rapid collapse and arise solely due to numerical effects. Truelove et al. (1997) pointed out that this can be avoided by sufficiently resolving the Jeans length through,

$$J = \frac{\Delta x}{\lambda_J} \leq 0.25 \quad (2.11)$$

where J is deemed the Jeans number, Δx is the size of the smallest cell, and λ_J is the Jeans length. The Jeans length must therefore be resolved by at least 4 cells on the highest level of refinement to avoid artificial fragmentation.

Turbulence and self-gravity were the first physics to be included into numerical simulations of cluster formation. The inclusion of turbulence is typically done in one of two ways. Those by Klessen and collaborators (as in Schmeja & Klessen (2004)) continuously force the velocity field over some range of scales setting up a quasistatic turbulent velocity field while others (as in Dale & Bonnell (2008)) initiate the simulation with a turbulent velocity field but include no further driving. Regardless of how the turbulence is initiated, some general conclusions can be drawn from these simulations. The most important conclusion is that the inclusion of turbulence significantly decreases the star formation efficiency per freefall time from 100% in the absence of turbulence to $\sim 30\%$ (Bate et al., 2003; Bonnell et al., 2008). As mentioned earlier, some turbulent simulations have been able to reproduce the high mass end of the IMF (Padoan & Nordlund, 2002b, 2005) but this is not the end of the story. For example, Bate & Bonnell (2005) found that the turnover in the IMF in turbulent simulations is dependent on the mass of the parent molecular cloud which is not seen in observations. This dependence can only be broken through the inclusion of more physics.

Simulations are revealing that clusters have a complex dynamical history. The turbulent fragmentation of a clump tends to give rise to subclustered regions which then undergo hierarchical merging to produce larger clusters (Clarke, 2010). This dramatically changes cluster morphology with time. Subclustered regions tend to be highly asymmetric likely due to the filament geometry out of which they form. As merging occurs between regions, the clusters take on a more spherical morphology through stellar-stellar interaction. Merger events can have a significant impact on the

form of the IMF because it provides massive stars with a large reservoir of gas from which it can accrete (Clarke, 2010). Merging events are quite common, as illustrated in Bate (2009) who showed that in a region of only $500 M_{\odot}$, there was a total of 5 subcluster mergers within 1.5 freefall times.

Newer generations of simulations have added different forms of stellar feedback which affect cluster formation to various degrees. The mechanical energy introduced by protostellar jets is found to have little effect on the total star formation efficiency even though it is driving turbulence on small scales (Hansen et al., 2012). Radiative feedback, through heating and ionization, has a more dramatic effect. Overall, the star formation efficiency per freefall time is decreased by a factor of two even though there is a small amount of triggered star formation (Offner et al., 2009). The formation of low mass objects is significantly suppressed as well, especially in the brown dwarf regime. This has a dramatic effect on the form of the IMF. A recent study by Krumholz et al. (2011) showed that the suppression of low mass fragmentation combined with continued accretion onto already forming stars can create a top heavy IMF.

The ionizing radiation does ionize the surrounding gas but not enough to stop the star formation process (Dale et al., 2005; Harper-Clark, 2011; Dale et al., 2012). The reason for this is the anisotropic structure inside the molecular clouds. The formation of stars and clusters takes place in filaments and the radiation produced by massive stars tends to escape into the low density voids perpendicular to the filament. Accretion onto the forming cluster can still occur along the filament. If the ionizing radiation is irradiating the cloud externally, however, it can have a dramatic

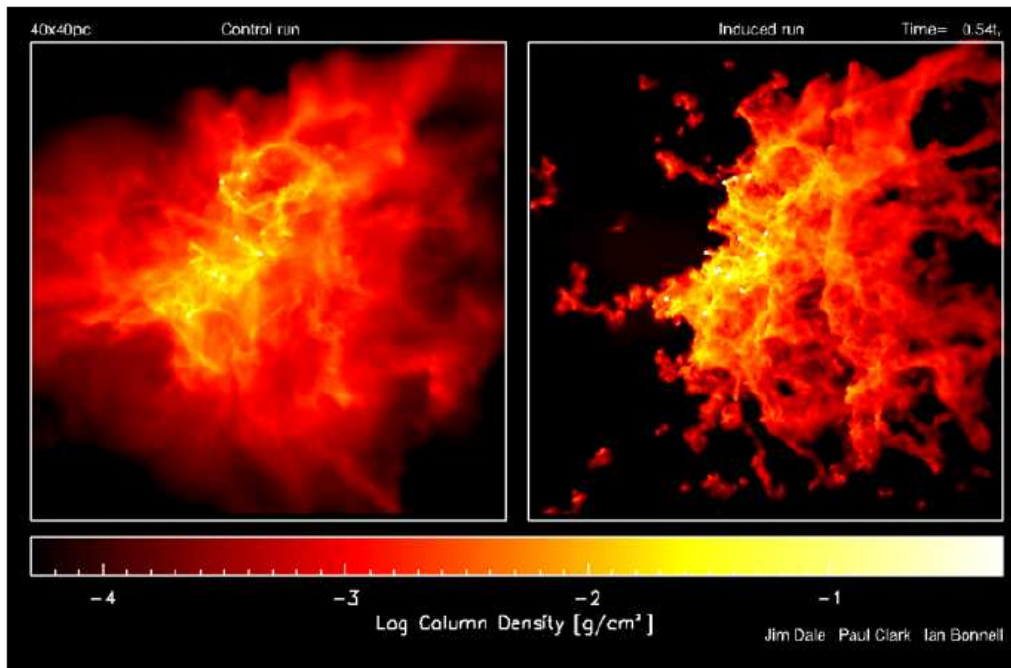


Figure 2.4: Column density plots showing the effect of external ionizing radiation (right) compared to a control run (left) from Dale et al. (2007). The incoming radiation effectively clears the gas from the forming protocluster.

effect on the morphology of the cloud as shown in Figure 2.4. In this case, the external ionizing radiation blows away the gas from the forming protocluster. This highlights the way in which ionizing radiation can cause negative feedback across an entire GMC; the first clusters that form can disperse the gas in their vicinity and externally irradiate clusters which are still forming in different regions of the cloud. We examine this possibility in our work.

There are still many open questions to be answered in numerical simulations of cluster formation. From a theoretical perspective, it is important to know which processes are the most important in controlling the star formation rate/efficiency in a molecular cloud and how different processes are interconnected. For this reason, we have chosen to examine the effects of turbulence and radiative feedback on the formation of stellar clusters on large spatial scales. To do this, we introduce a new technique which uses sink particles to represent entire stellar clusters whose radiative outputs are based on an IMF distribution, similar in principle to Harper-Clark (2011). The reason for this is two-fold; the computational cost will be significantly reduced due to the smaller number of particles involved meaning a more massive region can be simulated, and we know that the IMF is the final product of the star formation process so we can accurately represent the output of a cluster without knowing the internal dynamics. The inclusion of cluster particles will allow us to examine how a GMC is disrupted by radiative feedback and how this affects the cluster mass distribution. In the following Chapter, I describe the model for representing the radiative output of stellar clusters. The code we use and the implementation of

cluster particles is described in Chapter 4, followed by simulation results in Chapter 5. I end with some brief conclusions and directions for future work.

Chapter 3

Cluster Particle Model

The current chapter has been submitted to *Monthly Notices of the Royal Astronomical Society* and has been accepted pending moderate revision.

3.1 abstract We present a model for the radiative output of star clusters in the process of star formation suitable for use in hydrodynamical simulations of radiative feedback in GMCs. A clump of gas is converted to stars via the random sampling of the Chabrier IMF. A star formation efficiency controls the rate of star formation. We have completed a suite of simulations which follow the evolution of clumps with initial masses ranging from 0 to $10^5 M_{\odot}$ and accretion rates ranging from 10^{-5} to $10^{-1} M_{\odot} \text{ yr}^{-1}$. The stellar content of the clump is tracked over time which allows the aggregate luminosity, ionizing photon rate, number of stars, and star formation rate (SFR) to be determined. For a fiducial clump of $10^4 M_{\odot}$, the luminosity is approximately $4 \times 10^6 L_{\odot}$ with a SFR of roughly $3 \times 10^{-3} M_{\odot} \text{ yr}^{-1}$. We identify two regimes in our model. The accretion dominated regime obtains the majority of its gas through accretion and is characterized by an increasing SFR while the reservoir

dominated regime has the majority of its mass present in the initial clump and has a decreasing SFR. We show that our model can accurately reproduce the number of O stars, which dominate the radiative output of the cluster, observed in nearby clusters. We also plot the SFR in our clumps versus the clump mass at multiple times between 0.5 and 4 freefall times. We find a nearly linear relationship between SFR and mass with the powerlaw index ranging from 0.97 to 1.16. A timescale for star formation of 3 Myr is also found which is consistent with the age spread found in nearby clusters. We conclude that our model is an accurate and straightforward way to represent the output of clusters in hydrodynamical simulations with radiative feedback.

3.2 Introduction

The clustered nature of star formation plays an important role over a wide range of spatial scales. Since a large fraction of stars form in a cluster environment (Bressert et al., 2010), understanding the cluster formation process can provide insight into the origin of the initial mass function. On larger scales, star formation in clusters may play a central role in galactic scale feedback and the formation and destruction of giant molecular clouds (GMCs). Clusters are also interesting astrophysical objects in their own right since they can have a wide range of ages and masses while showing similar stellar contents.

Broadly speaking, the formation of a cluster can be thought of as the conversion into stars of a high density clump of molecular gas within a larger GMC. This process

can roughly be thought of in two separate steps. Firstly, the molecular gas in a clump becomes gravitationally unstable and fragments into protostars. Secondly, feedback mechanisms are responsible for shutting off the accretion onto the protostars and dispersing of the gas in the cluster's vicinity.

The conversion of molecular gas into fully formed stars is an inherently inefficient process (Lada & Lada, 2003). While feedback is certainly playing a role in the low efficiency, there are other proposed mechanisms that limit star formation. Initial turbulent velocity fields have been shown to significantly decrease the star formation efficiency per freefall time (Bate et al., 2003; Bonnell et al., 2008). However, given enough time, a turbulent molecular cloud will be converted to stars with a 100% efficiency in the absence of other mechanisms. Magnetic fields also provide a pressure support which can significantly decrease the star formation efficiency (Myers & Goodman, 1988). The process of feedback, however, does not just slow the star formation process but can shut off accretion to the cluster altogether. It is also important to consider because feedback affects the natal GMC since a clump and young cluster are not isolated from their surroundings.

The interplay of turbulence, gravity, and star formation in the early stages of cluster formation has been studied in detail (Klessen, 2001; McKee & Tan, 2003a; Ballesteros-Paredes et al., 2006; McKee & Ostriker, 2007). Recent *Herschel* studies emphasize that molecular clouds are highly filamentary (Schneider et al., 2012). Embedded young clusters in nearby molecular clouds appear at the joining points of several filaments (Schneider et al., 2012; Kirk et al., 2013). These are regions that can be fed by higher than average accretion rates (Banerjee et al., 2006). In a turbulent

medium, these points are dispersed so that monolithic collapse to form a cluster does not occur. The observations of the Orion cloud suggest that subclustering occurs across large regions of the cloud (Megeath et al., 2012) so that the formation of a cluster would involve the eventual merger of a significant number of subclusters.

There are several mechanisms that have been suggested as being responsible for shutting off accretion onto protostars and dispersing the remaining gas. These include stellar winds (Dale & Bonnell, 2008), radiation pressure (Krumholz & Thompson, 2012), ionization and heating of the surrounding gas (Dale et al., 2005; Peters et al., 2010; Klassen et al., 2012) and outflows from protostars in the presence of magnetic fields (Li & Nakamura, 2006; Maury et al., 2009). Of particular importance, and the focus of this paper, is feedback due to gas ionization and heating. Ionization is a vital process to include into numerical simulations because it is needed to reproduce observed HII regions.

To fully include radiative feedback effects requires a detailed radiative transfer scheme which can be computationally intensive. Nonetheless, the effects of radiative feedback from clusters have been examined on both small and large spatial scales (Dale et al., 2007; Peters et al., 2010; Bate, 2012; Dale et al., 2012; Klassen et al., 2012; Kim et al., 2012). Both approaches have advantages and disadvantages. Small-scale simulations of clusters, or multiple small clusters, simulate the formation of individual stars (Bate, 2012). This is advantageous because the radiative output of stars has been studied extensively through the use of stellar evolution codes. Also, since individual stars in these simulations can be resolved, studies aimed at the origin

of the IMF can be performed. However, these simulations require high resolution and are therefore computationally expensive.

Galactic scale simulations which include radiative feedback effects cannot resolve the formation of individual stars.

As a compromise in these galaxy-scale models, clusters are represented as a single object with a subgrid model to represent its radiative output (Tasker, 2011; Hopkins et al., 2012; Ceverino & Klypin, 2009). The clusters in these cases are typically given a fixed output that does not change with time. As an example, the luminosity of a cluster can be determined from its mass via an averaged IMF (Murray et al., 2010). This simplified approach misses key aspects of the star formation process.

As an attempt to bridge the gap between these two types of simulations, we present a model which can be used to represent the radiative output of a star cluster. This model was produced with the ultimate goal of being integrated into hydrodynamical simulations of cluster formation in giant molecular clouds.

Star forming cores that form individual stars are observed to follow a mass distribution (the so-called core mass function, CMF) that follows the IMF in structure, but displaced upwards in mass by roughly a factor of 3 (Rathborne et al., 2009; Könyves et al., 2010). So whatever the physical processes are in the gas that organize the CMF, we know that the outcome will resemble the IMF. A suggested star formation efficiency of around 30%, therefore, would give the distribution of star forming gas in a cluster forming region.

In our model therefore, we assume that the gas that accretes onto a cluster forming region is organized in this way. As the accretion brings fresh gas into a clump, more becomes available to be distributed amongst the star forming cores. We model this by randomly sampling the available gas reservoir, drawing from an overall distribution function that is the Chabrier IMF in order to decide the masses of the most recently formed stars. The mass spectrum of the protocluster clearly evolves with time, as gas is converted to stars from two gas sources - the initial gas mass of a clump, and the accreted mass from the external GMC. The model tracks the total cluster luminosity, number of ionizing photons, and the number and masses of stars contained in the cluster. These parameters can then be passed to a radiative transfer scheme to examine the effects of radiative feedback.

In section 3, we briefly highlight recent observations of embedded, star forming regions. Section 4 describes our basic model for cluster formation and is followed by results from a suite of simulations in section 5 which show that we are able to accurately capture the properties of young clusters.

3.3 Embedded star clusters: observations

The earliest phases of star formation are deeply embedded in molecular gas and therefore cannot be observed at optical wavelengths. However, molecular clouds are significantly less opaque at infrared wavelengths which allows for detailed surveys of embedded clusters with infrared telescopes such as *Herschel*. These studies indicate that embedded star formation accounts for a large fraction of all star formation

taking place in not only the Milky Way but other galaxies as well (de Grijs, 2010). Overall, the formation of the embedded cluster phase lasts approximately 2-4 Myr with the dissolution of the cluster through dynamical interactions and gas expulsion occurring within 10 Myr (Lada, 2010).

Observational studies are also revealing the complexity of cluster forming environments. *Herschel* observations in particular are highly filamentary (André et al., 2011; Schneider et al., 2012). Filaments can arise from a variety of processes including the passage of turbulent shocks in the ISM (Heitsch et al., 2001; Balsara et al., 2001; Boldyrev et al., 2002; Pudritz & Kevlahan, 2012), gravitational collapse (Hartmann & Burkert, 2007; Peters et al., 2012), and thermal instabilities (Vázquez-Semadeni et al., 2000). The largest areas of star formation occur at the junction of two or more filaments (Schneider et al., 2012). Growing clusters are fed by flow along the filaments (Kirk et al., 2013) which could prolong star formation since radiation and momentum feedback can be released into the lower density regions perpendicular to the filaments.

There is a large range of observed, embedded cluster masses and we have created our model with the goal of being able to reproduce this range. An example of a small embedded cluster is the Serpens South star forming region. This is a young cluster which currently contains approximately 90 young stellar objects (YSOs) which are being actively fed by filamentary flows (Kirk et al., 2013). An intermediate mass example is the well-studied Orion Nebula Cluster (ONC) which is the nearest site of massive star formation. This is a young cluster (a few Myr old) with a present day mass of $\sim 4800 M_{\odot}$ (Hillenbrand & Hartmann, 1998) and about 2200 stars contained

within a radius of 2pc from its centre (Pudritz, 2002). Unlike Serpens South, the ONC is the host to massive star formation with roughly 5 stars having masses greater than $16 M_{\odot}$ which fall in the O star range (Hillenbrand, 1997). As mentioned earlier, there is strong evidence for subclustering in the ONC (Megeath et al., 2012). An extremely massive example would be R136 which is the core of a “super star cluster” at the centre of the 30 Doradus complex. *Hubble Space Telescope* imaging has revealed over 3500 stars in the centre of R136 with more than 120 of these stars being blue and more luminous than $M_v \sim -4$ (Massey & Hunter, 1998). This cluster has stellar densities which are 100-300 times more dense than any other cluster in the Milky Way or the LMC (Hunter et al., 1996) and contains several stars whose masses exceed $100 M_{\odot}$ (Massey & Hunter, 1998).

A high density clump of molecular gas is required to form an embedded star cluster regardless of its mass. Observations of star-forming and star-less clumps suggest that a number density of 10^4 cm^{-3} is required to start the star forming process (Lada & Lada, 2003). The efficiency with which clouds are converted to stars is still in dispute. Individual clouds in our Galaxy have a mean density of a few times 10^2 cm^{-3} and have global star formation efficiencies ranging from 2% to 8% (Kennicutt & Evans, 2012). Embedded clusters have higher efficiencies between 10-30% (Lada & Lada, 2003). Hydrodynamical simulations indicate that the actual star formation rate may need to be as high as 70% to have stable, bound clusters (de Grijs, 2010).

An important quantity which can be compared to our work is the star formation rate (SFR). The star formation rate in local clouds can span several orders of mag-

nitude from 10^{-6} to $10^{-2} M_{\odot} \text{ yr}^{-1}$. The well studied Orion A cloud is found to have a star formation rate of $7.15 \times 10^{-4} M_{\odot} \text{ yr}^{-1}$ (Lada et al., 2010a). Recent studies of the massive star forming region G29.960.02 indicate a current star formation rate 0.001-0.008 $M_{\odot} \text{ yr}^{-1}$ (Beltran et al., 2013) which is also consistent with Galactic HII regions (Chomiuk & Povich, 2011). The mass of G29.960.02, a star-forming region in the Milky Way, is given as $\simeq 8 \times 10^4 M_{\odot}$ (Beltran et al., 2013) which will be a useful comparison to our models. Our model will also be compared to the more massive ($\approx 3 \times 10^5 M_{\odot}$) G305 star forming cloud, located roughly 4 kpc away in the Scutum-Cruz arm of the Milky Way, with formation rates of 0.01-0.02 $M_{\odot} \text{ yr}^{-1}$ (Faimali et al., 2012).

3.4 A basic model for cluster formation One of the most important aspects of radiative feedback of a young forming cluster on its surrounding host GMC is the shutting off of the accretion flow into the cluster forming region. To examine the radiative feedback effects of clusters on their surroundings, the cluster particles must be assigned the correct, combined radiative output of all its member stars as star formation proceeds. Cluster formation begins in a clump that has reached a critical density. Therefore, one input for a theory or subgrid model is how massive the original gas reservoir was at the moment that stars begin to form. Star formation proceeds as gas accretes onto this original dense region. Secondly, as its mass increases, the gravitational attraction of more material from the surrounding cloud will increase. The third step, ultimately, is the feedback from the cluster which helps to shut off the accretion flow onto the cluster forming clump.

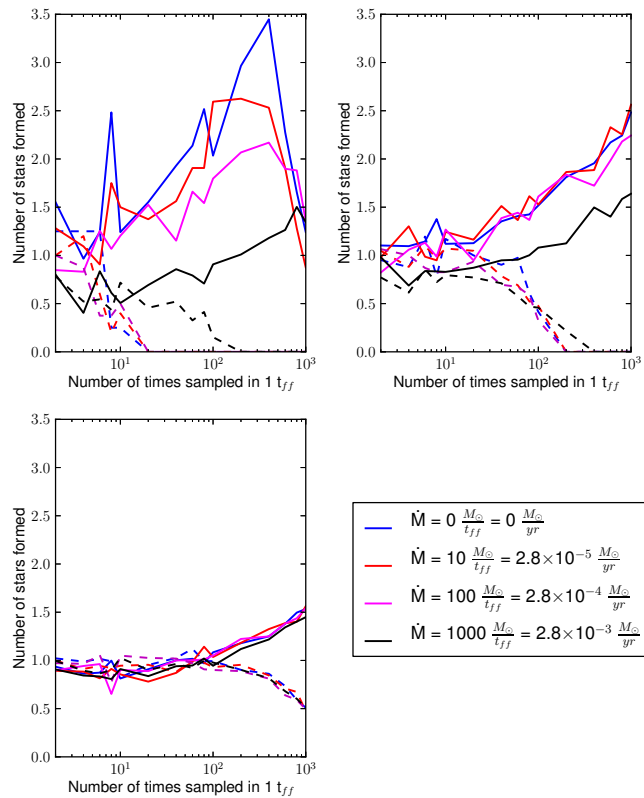


Figure 3.1: Plots of the number of stars relative to the expected number versus sampling frequency for clusters with different initial masses and different constant accretion rates. The initial masses of the cluster are 100 (top left), 1000 (top right), and 10000 (bottom left) M_{\odot} . The solid lines represent stars less than $1 M_{\odot}$ and dotted lines represent stars greater than $1 M_{\odot}$.

Therefore, the modeling needs to address two questions. How should the original gas reservoir be divided into stars? Second, how should the ongoing accreted gas be divided? The most straightforward way to address the former question is to divide the mass into stars at some prescribed efficiency according to an IMF. This ignores the effect of prestellar evolution but has the advantage of producing a cluster with the observed distribution of stellar masses. While including prestellar evolution into the model may be more physically realistic, we argue that it is acceptable to place the stars directly on the main sequence since our simulations will run much longer than the prestellar evolution phase. Since higher mass stars evolve onto the main sequence rapidly, and the high mass stars are the largest contributors in terms of ionizing feedback, ignoring prestellar evolution is a justified approximation. Further support comes from Klassen et al. (2012) who compared the effects of radiative feedback from stars with prestellar evolution and those without it. The authors found that there was not a significant difference between the two cases.

Since the cluster will be actively accreting gas until feedback effects stop the inflow, any added mass has to be dealt with accordingly. This gas can either be added to existing stars or used to form new stars. While there are theoretical arguments for the accretion rate onto individual stars varying as M^2 (Bondi, 1952; Krumholz et al., 2006b; Throop & Bally, 2008) in the absence of turbulence, the fraction of gas accreted by existing stars and the fraction of gas used to form new stars is unknown. To avoid adding uncertain parameters into our model, we therefore assume that a fraction of the available gas is only used to form new stars.

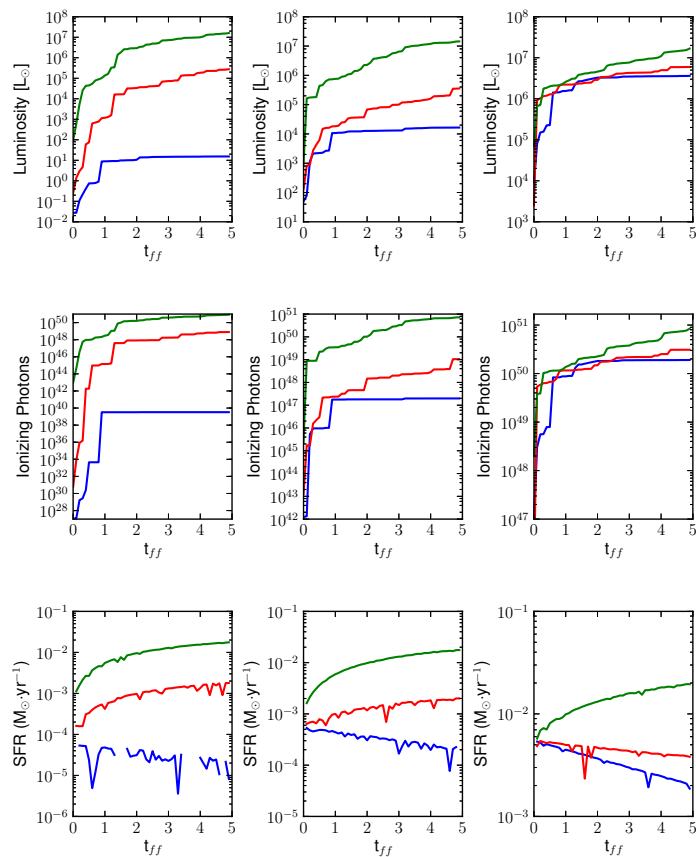


Figure 3.2: A subset of our data showing the luminosity, number of ionizing photons, and the star formation rate. Blue, red, and green lines represent accretion rates of 0, 2.8×10^{-3} and $2.8 \times 10^{-2} M_{\odot} \cdot \text{yr}^{-1}$, respectively. The columns, from left to right, represent initial clump masses of 100, 1000, and 10000 M_{\odot} .

With this in mind, the concept of our model works as follows. A clump, assumed to be at the threshold density for cluster formation, forms and its mass is specified beforehand. From observational work, a number density of 10^4 cm^{-3} is typical of a star forming clump (Lada & Lada, 2003). We therefore adopt this value as our density threshold for the formation of a cluster particle. The mass of the clump is initially divided into two categories; gas mass which will be used to form stars, and the leftover gas which will hereafter be designated as the 'reservoir'. The gas used for star formation is then distributed to main sequence stars via an IMF. Individual stellar masses are recorded so that the total mass of the clump in stars is known at any given time. If the random sampling of the IMF results in a star which has a mass greater than the total mass available for star formation then sampling is stopped and any remaining gas is added back to the reservoir. This process repeats by taking a fraction of the reservoir mass and converting it to stars. Over a sufficiently long time, all the mass in the cluster will be in the form of stars. Any mass accreted by the clump, with an accretion rate specified by the user, is added to the reservoir. It should be noted that accretion in this context refers to the replenishing of clump mass rather than accretion onto individual protostars.

Our star forming clumps are allowed to grow in mass through accretion but no mass loss is included. A physical motivation for our gas reservoir is required to justify this assumption. We posit that the reservoir gas in our subgrid model is in a dense enough state to remain bound over long timescales even in the presence of stellar feedback. This has indeed been shown in simulations. Dale et al. (2005) showed that the inclusion of radiative feedback into cluster formation simulations

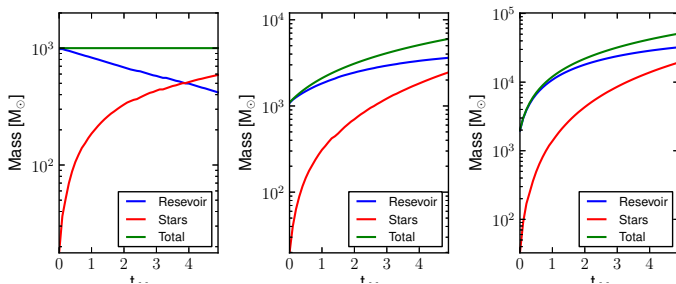


Figure 3.3: The total gas mass, the mass in stars, and the reservoir mass as a function of time for an initial clump mass of $1000 M_{\odot}$. The panels from left to right represent models with an accretion rate of 0, $2.8 \times 10^{-3} M_{\odot} \text{yr}^{-1}$, and $2.8 \times 10^{-2} M_{\odot} \text{yr}^{-1}$.

resulted in collimated ionized outflows which are released perpendicular to the dense filaments from which they are forming. Even though these outflows accelerate a small fraction of the gas to high velocities, this is *not* sufficient to unbind the bulk mass of the clump. In the case of external ionizing radiation, as discussed in Dale et al. (2007), no dense star forming cores are disrupted. There is also evidence for triggered star formation in these simulations suggesting that even if the gas is disrupted due to stellar feedback, it may still form stars in a separate region of the cloud. We therefore assume our gas reservoir is in a clumpy and filamentary state, preventing its disruption via stellar feedback, meaning it can still form stars.

To populate the cluster with stars, an IMF is randomly sampled with a Metropolis-Hastings algorithm. This algorithm is an example of a Markov Chain Monte Carlo method and works by generating a random walk and uses a specified probability distribution to either accept or reject the proposed move. More specifically, the acceptance ratio, α , is calculated which is the ratio of probabilities between the proposed

move and the previously accepted move. The acceptance ratio is then interpreted as the probability that the move is accepted (if $\alpha \geq 1$ it is accepted automatically). We use the Chabrier IMF (Chabrier, 2005) as our input probability distribution which is expressed as,

$$\xi(\log m) = \begin{cases} 0.093 \times \exp\left\{\frac{-(\log m - \log 0.2)^2}{2 \times (0.55)^2}\right\}, & m \leq 1 M_{\odot} \\ 0.041 m^{-1.35 \pm 0.3}, & m > 1 M_{\odot}. \end{cases} \quad (3.1)$$

Randomly sampling the IMF introduces stochastic effects into our model. The stars are allowed to have masses between 0.01 and 100 M_{\odot} . The lower limit is below the brown dwarf limit but we are concerned with the effects of the radiation field and brown dwarfs will not contribute significantly to the overall luminosity. The luminosity of a star is based on its mass via the function found in Tout et al. (1996).

The star formation efficiency of 20% per freefall time is used in order to control the rate of star formation (Lada & Lada, 2003). The freefall time is given by,

$$t_{ff} = \sqrt{\frac{3\pi}{32G\rho}} \quad (3.2)$$

which results in a value of 0.36 Myr assuming the density threshold of 10^4 cm^{-3} discussed earlier. It should be noted that our star formation efficiency only reflects what is happening inside the cluster forming clump. The majority of the gas in a

molecular cloud is at much lower density (on average about 100 particles per cm^{-3}) and may not end up in clusters meaning that the global star formation efficiency can be much less than 20%. Since the IMF is not necessarily being sampled only once per freefall (see below), the fraction of total gas that is converted to stars every timestep is given by $f = M_{res}\epsilon n/M_{tot}$ where M_{res} is the reservoir of gas inside the cluster which has not been converted to stars, ϵ is the fraction of reservoir gas converted to stars per freefall time, n is the number of times sampled in a freefall time, and M_{tot} is the total mass of the clump and cluster. The mass of all stars formed is tracked so that at any given time we know how much mass is tied up in stars and how much gas is available for future star formation.

Recording the masses of all stars formed allows the ensemble properties of the clusters to be determined. The total cluster luminosity is the sum of the individual stellar luminosities which are determined through the analytic formulas provided by Tout et al. (1996). These formulas provide the temperature and radius of main sequence stars from their masses which is then used to calculate the stellar luminosity. We also calculate the the ionizing photon rate, in s^{-1} , from the cluster which is again the sum of the individual stellar rates. The ionizing photon rate is found by directly integrating a blackbody distribution.

How often the IMF is sampled for building new stars in a cluster forming clump can have a significant impact on the cluster's properties and evolution. If sampling is done infrequently (ie. a small n) then a larger amount of gas available for star formation will be converted to stars, but the luminosity will have large and discontinuous jumps. On the other hand, if the IMF is sampled too frequently then the

amount of gas that is being converted to stars each timestep will be small meaning that high mass stars cannot be formed. This would lead to a bias towards low mass stars. It is therefore necessary to find the smallest value of n which still reproduces the IMF.

To examine the effect of changing the IMF sampling rate, multiple models were run over one freefall time with varying initial clump masses and accretion rates. We stress that the accretion rates are constant over time and were chosen to be representative of the actual accretion rates onto clusters. In a real cluster forming environment, the resulting radiation field would eventually act to reduce the accretion rate by feedback. This step is handled in our full simulations of feedback onto the surrounding GMC gas. The results are shown in Figure 3.1. The plots show the number of low mass stars ($< 1 M_{\odot}$) and high mass stars ($> 1 M_{\odot}$) as a function of the sampling rate. The number of stars is shown relative to their expected numbers. The expected number of stars is found by directly integrating the Chabrier IMF for a cluster which contains the same mass in stars. It can be seen that the number of stars deviates from the expected numbers at high sampling frequencies in all cases. The divergence point, however, does not occur at the same place and increases in sampling frequency with increasing mass. This is easily understood in terms of the available mass used to form stars at the time of sampling. As the sampling rate increases, the amount of gas being converted to stars decreases.

It can be seen from the figure that there is a large amount of scatter in the $100 M_{\odot}$ case. This is due to the smaller number of total stars formed in this case. Therefore,

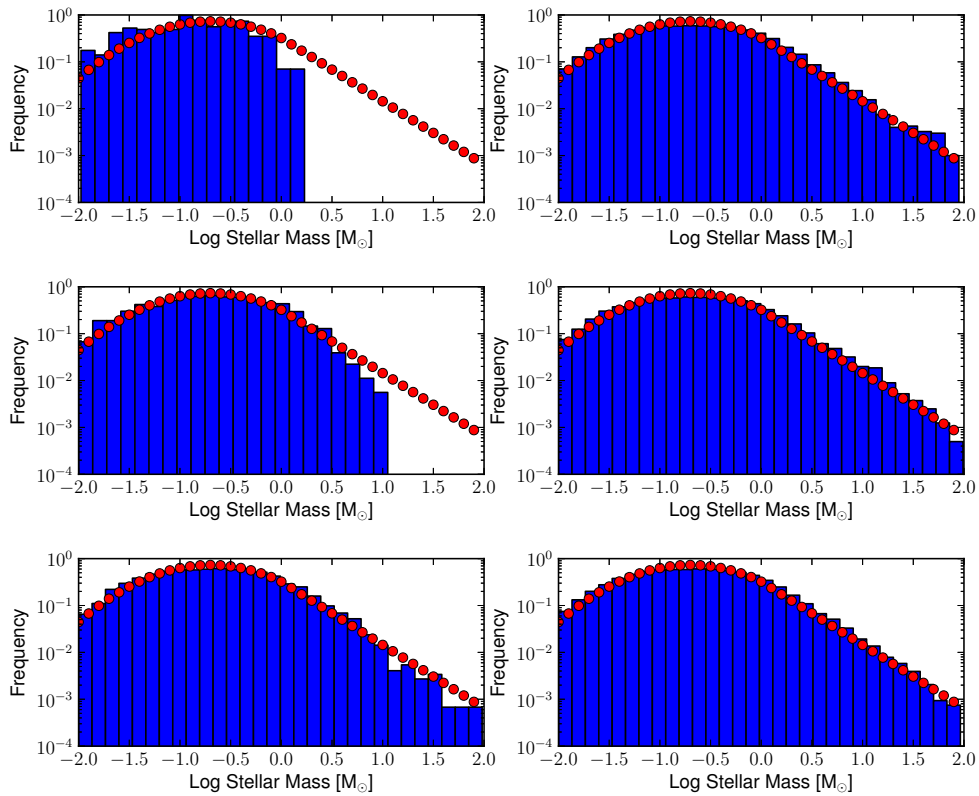


Figure 3.4: The resulting mass function for models with no accretion (left) and an accretion rate of $2.8 \times 10^{-2} M_{\odot} \text{ yr}^{-1}$ (right) for initial clump masses of 100 (top), 1000 (middle), and 10000 (bottom) M_{\odot} . The red circles represent the normalized Chabrier IMF.

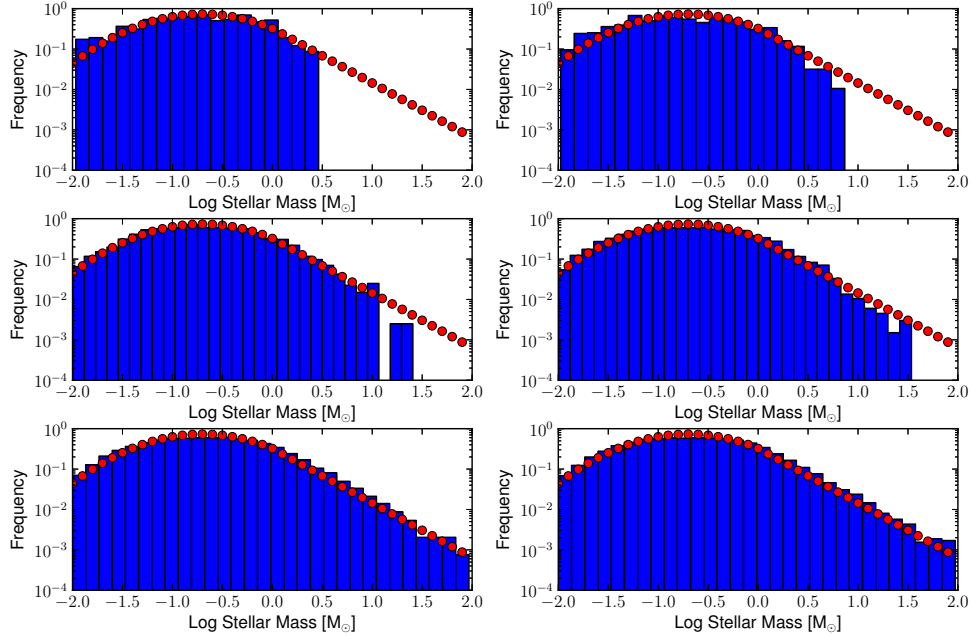


Figure 3.5: The resulting mass function for models with the same final clump mass but have either accreted all the mass (left) or had no accretion and the mass was present initially (right). From top to bottom, the final clump masses are 500, 5000, and 50000 M_{\odot} . The red circles represent the normalized Chabrier IMF.

the formation of a single high mass star has a larger impact in comparison to the higher clump mass cases.

Based on Figure 3.1, we have chosen to sample the IMF 10 times per freefall time which corresponds to approximately 36 kyrs. This sampling rate still reproduces the number of high and low mass stars for all mass ranges. As shown in the next section, this sampling rate also reproduces the correct number of O stars which are the most important stellar population with respect to ionizing feedback. It should be noted

that the chosen sampling time is less than the time it takes for a massive star to form and reach the main sequence. If the sampling frequency was greater than this time then the ionizing luminosity of the cluster would be underestimated between samplings.

In the following section, we present the result of a suite of models that were run with different initial cluster masses and different accretion rates.

3.5 Results

To examine the longterm behaviour of our model, we ran multiple simulations for various initial clump masses and accretion rates. All models were run for 5 freefall times or $\simeq 1.8$ Myr. The initial clump masses ranged between 0 and $10^5 M_{\odot}$. At $0 M_{\odot}$, the evolution is tied only to the mass that it accretes. The high initial clump mass of $10^5 M_{\odot}$ was chosen to be representative of a protoglobular cluster.

The accretion rate into the clump was chosen to be constant and had values ranging from $0 M_{\odot} t_{ff}^{-1}$ to $10^5 M_{\odot} t_{ff}^{-1}$ (or $\approx 2.8 \times 10^{-1} M_{\odot} \text{ yr}^{-1}$). These rates were chosen to be representative of realistic cluster accretion rates. Observational studies have shown that high mass protostars have accretion rates up to 10^{-4} - $10^{-3} M_{\odot} \text{ yr}^{-1}$ (Fuller et al., 2005; Beltran et al., 2006). Therefore, our highest accretion rate roughly corresponds to a cluster which is forming multiple large mass stars. It should be noted that a cluster will not have a constant accretion rate especially over 5 freefall times. However, a constant accretion rate is the easiest to implement and can still provide information on how physical properties of our clusters vary depending on accretion

rate. When this model is used in hydrodynamical simulations, the accretion will be determined by the environment surrounding the cluster and not put in manually as is done here.

To ensure that our model is behaving as expected, we chose a subset of our data and plotted (see Figure 3.2) the luminosity, number of ionizing photons, and the star formation rate (SFR). These quantities were chosen as useful comparisons to observational data. The initial clump masses in Figure 3.2 are 100, 1000, and 10000 M_{\odot} from left to right. The accretion rates shown in blue, red, and green are 0, $2.8 \times 10^{-3} M_{\odot} \text{ yr}^{-1}$, and $2.8 \times 10^{-2} M_{\odot} \text{ yr}^{-1}$, respectively.

The initial masses and accretion rates were chosen to represent a wide range of clusters. The final clump masses cover a range from 100 M_{\odot} to 60000 M_{\odot} , the range of luminosities is 10 L_{\odot} to $10^7 L_{\odot}$, and ionizing fluxes ranging from 10^{40} to 10^{51} s^{-1} . The SFRs at low cluster masses show significant variability which can be attributed to the stochastic sampling of the IMF. The discontinuous lines in the SFR plots indicate that no star formation has occurred during those timesteps.

There are two general trends to note in Figure 2. The first is that a higher accretion rate results in higher values for all three quantities plotted, as expected. Second is that as the initial clump mass increases the final luminosity and number of ionizing photons begin to converge. This is due to the large initial gas reservoir available which outweighs the effect of the smaller accreted mass.

Since our model will be used to represent the radiative feedback of clusters, it is important to verify that the expected number of ionizing photons are being produced.

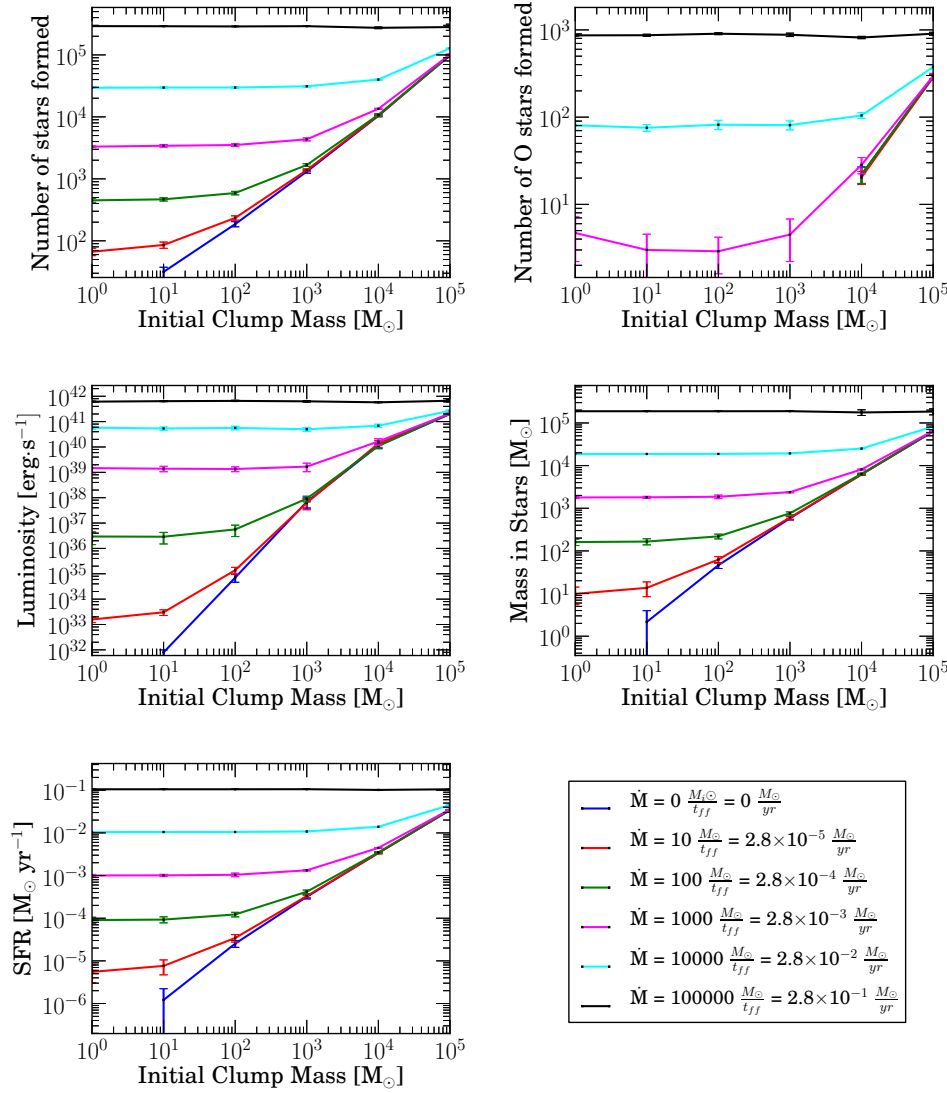


Figure 3.6: The total number of stars, the number of O stars, and the final luminosity of runs with varying accretion rates and initial clump masses. The points represent the average of all runs and the error bars represent one standard deviation.

The number of ionizing photons ($E_{phot} > 13.6$ eV) for clusters has been calculated in previous population synthesis models which include the effects of stellar evolution and metallicity (Smith et al., 2002; Sternberg et al., 2003). Our model reproduces their cited values to within an order of magnitude for similarly sized clusters. For example, an impulsive burst of star formation with a total mass of $10^5 M_{\odot}$ and an upper IMF limit of $120 M_{\odot}$ results in an ionizing photon rate of $\sim 8 \times 10^{51} \text{ s}^{-1}$ in Sternberg et al. (2003). The large jumps in the number of ionizing photons can be traced back to the emergence of individual massive stars. For example, the steep rise in the model with an initial mass of $1000 M_{\odot}$ and no accretion (blue line in centre panel of Figure 3.2) is due to the formation of a $11.2 M_{\odot}$ star. It should be noted that our model does not include stellar deaths so the luminosity and number of ionizing photons can only increase with time.

The star formation rates shown in Figure 3.2 span a few orders of magnitude from 10^{-5} to $10^{-2} M_{\odot} \text{ yr}^{-1}$. Recent studies of the massive star forming region G29.960.02 ($\approx 8 \times 10^4 M_{\odot}$) indicate a current star formation rate 0.001 - $0.008 M_{\odot} \text{ yr}^{-1}$ (Beltran et al., 2013). This roughly corresponds to our model with an initial mass of $10000 M_{\odot}$ and an accretion rate of $10000 M_{\odot} \text{ yr}^{-1}$ (green line in bottom right panel) which has a final mass of $60000 M_{\odot}$ after 5 freefall times. The star formation rate for this case ranges from 0.005 - $0.02 M_{\odot} \text{ yr}^{-1}$ and therefore agrees with the observation initially. Our model also agrees with the more massive ($\approx 3 \times 10^5 M_{\odot}$) G305 star forming cloud with formation rates of 0.01 - $0.02 M_{\odot} \text{ yr}^{-1}$ (Faimali et al., 2012). The RCrA star forming cloud is an example of a smaller region which has a mass of roughly $1100 M_{\odot}$ and has a SFR of $2.5 \times 10^{-5} M_{\odot} \text{ yr}^{-1}$ (Lada, 2010). Our model with an

initial mass of $1000 M_{\odot}$ and no accretion (blue curve in middle, bottom panel) shows a SFR which is higher by an order of magnitude. It should be noted that there is a wide range in SFRs between clouds with similar mass and since our model does not include accretion onto forming protostars, we provide an upper limit to the SFR.

The evolution of the star formation rate with time shows two recurring trends: those with an increasing SFR, and those with a decreasing SFR. The difference between the two trends is due to the amount of gas in the reservoir. The cases showing a decreasing SFR have total accreted mass which is less than the initial clump mass and is therefore reservoir dominated. This leads to a decreasing reservoir mass. Conversely, all cases which have an increasing SFR are accretion dominated. This leads to a build up of the reservoir mass and the corresponding increase in the SFR. As an example, consider the middle panel in Figure 3.2 showing the SFR. This panel represents an initial clump mass of $1000 M_{\odot}$. The case with zero accretion shows a decreasing SFR while the cases with $\dot{M} = 1000$ and $10000 M_{\odot} t_{ff}^{-1}$ have an increasing SFR.

Figure 3.3 shows how the total mass of the star forming region, the mass in stars, and the reservoir mass evolve with time. It can be seen that the SFR has qualitatively similar behaviour to the reservoir mass which confirms that the interplay between accretion and initial clump mass plays an important role in determining the cluster's properties.

The mass functions plotted in Figure 3.4 show that the powerlaw tail extends to higher masses when starting with a higher mass clump and no accretion. While the

probability of forming a massive star is the same between cases, the extra condition that there must be enough available mass to form massive stars is responsible for the broadening of the mass function. The cases with an accretion rate of $2.8 \times 10^{-2} M_{\odot} \text{ yr}^{-1}$ do not show this behaviour. This is because all models have accreted the same amount of gas and therefore show a similar mass function. Since this accretion rate is typical of actual clusters, this suggests that accretion into a clump may be partly responsible for the universality of the IMF since it provides enough mass to have a fully sampled IMF.

It is important to note that even though we are using the Chabrier IMF as a probability density function in this work, the resulting mass function will not necessarily be identical to the IMF. The imposed condition that there must be enough mass available during each sampling to form the randomly selected stars means that only the higher mass clumps can form massive stars. In the case of lower mass clumps, massive stars cannot form so the high mass tail of the mass function is truncated at a value less than the maximum stellar mass of $100 M_{\odot}$. The stars that do form, however, will follow the Chabrier IMF but the distribution will not entirely cover the allowed range of stellar masses.

While Figure 3.4 shows that a large clump accretion rate results in a similar IMF independent of initial clump mass, it is difficult to draw further conclusions since all clumps shown have a different final mass. Therefore, we have plotted the resulting IMF of models which have the same final clump mass but either got their mass solely through accretion (left) or solely as the initial mass of the clump (right) in Figure 3.5.

These represent the extremes of the accretion dominated and the reservoir dominated regimes.

The main difference between the two regimes is the extent of the high mass end of the IMF. The cases where all the mass was present in the initial clump forms more high mass stars. Conversely, cases where the majority of the clump mass is accreted have fewer high mass stars. We are only showing a representative case in Figure 3.5 but this trend holds in general. This result highlights the importance of how a clump or cluster gets its mass since we have shown that the resulting IMF can vary depending on whether accretion is present. The difference can be attributed to the total mass in stars present at the end of the simulation. Reservoir dominated cases are found to have significantly higher masses in stars than accretion dominated cases. As an example, take the case with a total mass of $5 \times 10^4 M_{\odot}$. The case with accretion has $\sim 19,000 M_{\odot}$ in stars compared to $\sim 32,000 M_{\odot}$ for the case without accretion even though both clumps have the same total mass. This also translates to a lower SFR and a higher star formation timescale in accretion dominated cases. Radiative feedback may therefore play less of a role early on in the star formation process for low mass clumps which are actively accreting gas.

It is important to note that the differences between the reservoir dominated and accretion dominated regimes decrease with increasing clump mass. This is because there is enough gas present to have a fully sampled IMF regardless of how the mass was obtained (shown in the bottom panel of Figure 3.5).

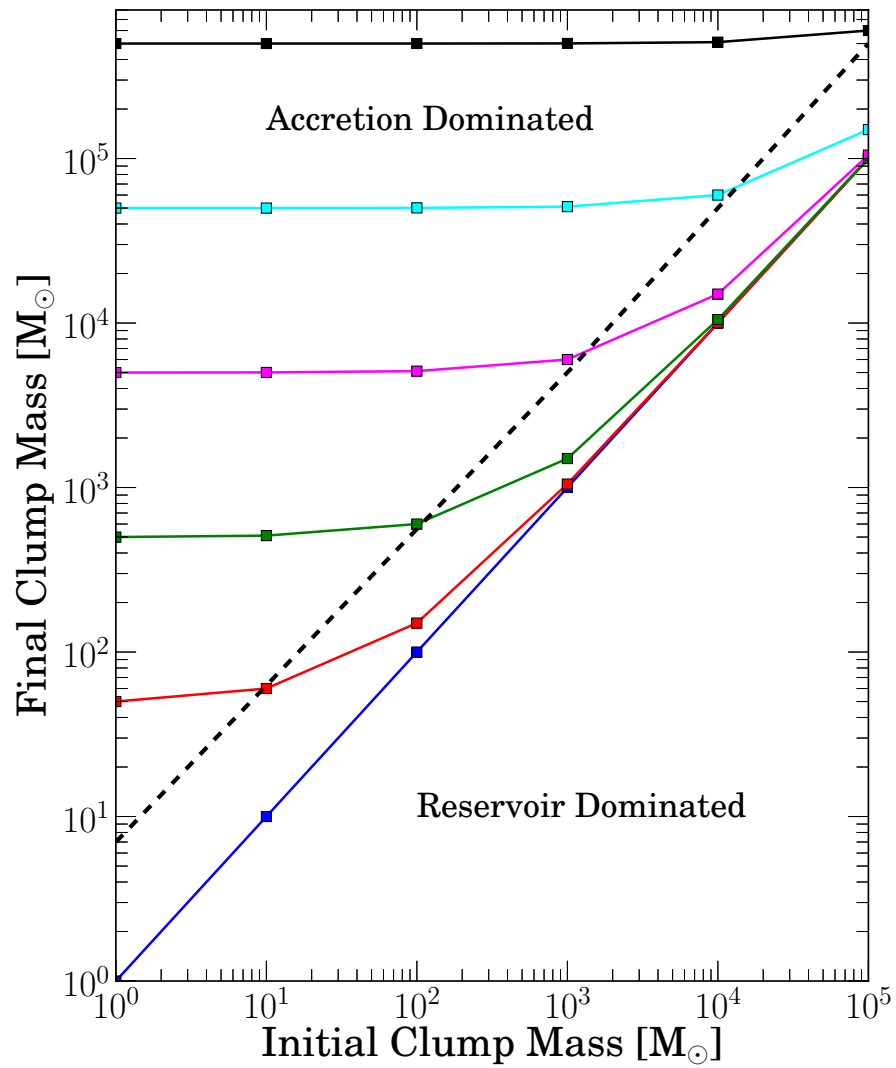


Figure 3.7: A reference figure showing the final clump masses for the models run in Figure 3.6 with the same colour coding. The dotted black line shows separates the accretion and reservoir dominated regimes.

The analysis presented above is based on single model runs. Since there is a stochastic component related to the sampling of the IMF, it is useful to quantify how results vary between runs with identical input parameters.

In Figure 3.6, we plot the total number of stars formed, the number of O stars formed, the resulting luminosity, the total mass in stars, and the SFR for models with varying initial clump masses and accretion rates. The code was allowed to run for 5 freefall times as above. Models with accretion rates between 0 and $2.8 \times 10^{-2} M_{\odot} \text{yr}^{-1}$ were run 100 times each and the highest accretion rate of $2.8 \times 10^{-1} M_{\odot} \text{yr}^{-1}$ was run 10 times. The average values and corresponding standard deviations are plotted in Figure 3.6. It can be seen that our model covers a wide range of cluster types, ranging from small clusters with less than 100 stars to the globular cluster regime. There is variation between runs with identical input parameters but the results are typically consistent to within a factor of 3. It can be seen from these plots that all three quantities increase with accretion rate as expected. There is also a flat region that occurs at low initial clump masses for all quantities. The size of the flat region, however, increases with increasing accretion rate.

Again, this can be understood in terms of the relative importance of initial clump mass and the accretion rate. The accretion dominated cases show little variation in the quantities. This is because the initial mass is a small fraction of the final mass so its effect is ‘washed out’. Only when the accreted mass becomes significantly smaller than the initial clump mass do the quantities begin to vary. Take, for example, the case with an accretion rate of $2.8 \times 10^{-3} M_{\odot} \text{yr}^{-1}$. The total accreted mass after 5 freefall times is $5000 M_{\odot}$. All quantities remain constant for cases where the initial

mass is $\leq 1000 M_{\odot}$. There is an increase in all quantities when the initial clump mass is $10^4 M_{\odot}$, confirming that the interplay between initial clump mass and accreted mass is important in determining the cluster's properties.

To make the distinction between accretion and reservoir dominated regimes more clear, we have plotted the final clump mass versus the initial clump mass in Figure 3.7. This allows one to determine the properties given in Figure 3.6 for a region with a desired final mass. The dotted black line roughly shows the transition between the accretion dominated and reservoir dominated regimes. Figure 3.7 is qualitatively similar to the plots shown in Figure 3.6 suggesting that these quantities scale directly with the clump mass.

We have also examined how the SFR scales with clump mass. The SFR is chosen because it has been measured in a variety of star forming environments over scales ranging from individual clumps to entire GMCs. Rather than plotting the final clump mass, however, we have chosen to plot the instantaneous SFR versus the clump mass at 0.5, 1, 1.5, 2, 3, and 4 freefall times to give snapshots of the evolution at several stages. The results for all accretion rates are shown in Figure 3.8. As in Figure 3.6, the error bars are the resulting standard deviations from 100 runs with identical input parameters. The distribution was fit with a powerlaw given by,

$$SFR = const \cdot M^{\alpha} \tag{3.3}$$

and the resulting index values shown in Figure 3.8 fall in the range

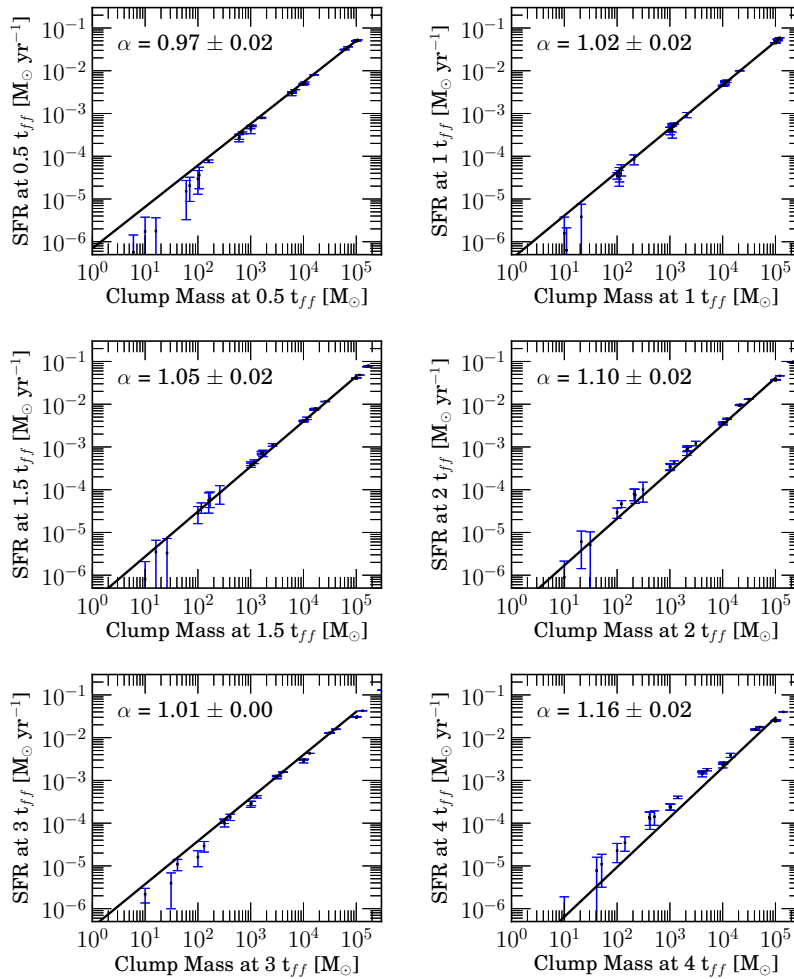


Figure 3.8: The instantaneous SFR as a function of total clump mass at 2 freefall times. Error bars represent the resulting standard deviations from 100 identical runs. The α parameters shown in the plots are the resulting indexes from powerlaw fits to the data. The error on α , obtained through the fitting, is also shown.

$$\alpha = 0.97 - 1.16. \quad (3.4)$$

There are several studies which show that the observed SFR is linearly related to the dense gas mass. Within our own galaxy, Wu et al. (2005) examined the far infrared (FIR) luminosity versus the HCN luminosity in nearby clouds. HCN requires dense gas ($n \geq 10^4 \text{ cm}^{-3}$) in order to be visible, and the FIR luminosity traces star formation. The authors found that there is a linear relation between the two quantities. This relation has also been found in normal spiral and starburst galaxies by Gao & Solomon (2004). These results are also supported by Lada et al. (2010b) who found that the number of YSOs is linearly related to the gas mass above a given density threshold. The data suggests that our model can reproduce the behaviour of clumps and clusters with a wide range of physical characteristics.

Figure 3.8 is also showing that the index α increases slowly with time, most likely due to the accelerating SFR in accretion dominated cases and the decreasing SFR in reservoir dominated cases. The very low mass clumps are certainly reservoir dominated, and therefore have decreasing SFR with time, while the highest mass clumps are accretion dominated. The increasing SFR on the high mass end together with the decreasing SFR on the low mass end result in a steepening of the slope.

The assumption that we convert a fixed amount of gas to stars, 20% of the available reservoir gas per freefall time, would suggest that a linear relationship between the SFR and clump mass is a direct underlying result of our model. There are reasons, however, why the linear dependence is unexpected and therefore significant.

Since we are converting 20% of the *available reservoir gas* rather than 20% of the total cluster mass (reservoir gas plus stars), the SFR is sensitive to the accretion history of the cluster. This is most easily understood in terms of clusters that have identical masses but are either in the extreme accretion dominated or reservoir dominated regime. In the accretion dominated regime, the amount of gas in the reservoir is increasing and, as shown earlier, so is the SFR. The opposite is true for the reservoir dominated regime. Therefore, two clusters with identical masses can have different amounts of reservoir gas which translates to different SFRs. This could lead to a non-linearity in the SFR vs clump mass plots. The condition that, in a given timestep, there must be enough available gas to form the randomly selected star can also lead to non-linearities especially in the case of low mass clumps. It can be seen that there is a slight departure from the linear behaviour of the plots seen in Figure 3.8 at the low mass end. These points are consistently below the line, likely due to the lack of massive star formation. Since these low mass clumps are not converting a significant amount of gas to stars each timestep, a large fraction of randomly selected stars cannot form. This provides a useful prediction for the SFR in small mass clumps; namely, there should be a departure from a linear dependence at low clump masses.

As a further comparison to observed star-forming clumps, in Figure 3.9 we have plotted the SFR versus clump mass at 2 freefall times and overplotted the observed SFRs inferred by Lada et al. (2010a) for nearby star-forming complexes. We have only shown our data at $2 t_{ff}$ because the same general trend holds for the SFR at any time. We find that our data is consistently higher than the observed SFRs for

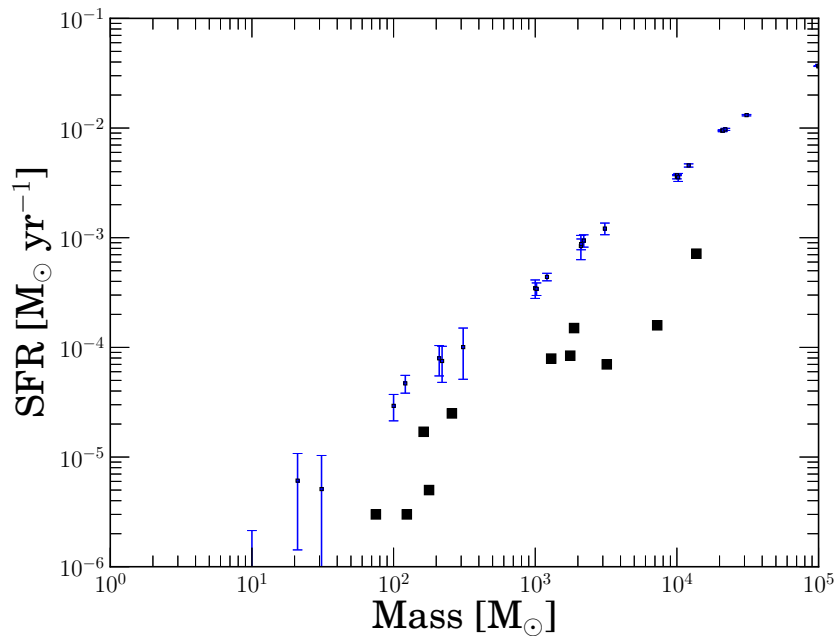


Figure 3.9: The SFR versus clump mass for this work, shown in blue, and observations presented in Lada et al. (2010a), shown in black. The observed SFRs are systematically lower compared to our model.

all points and do not agree within error. Our data does agree with the measured values to within an order magnitude. We have attributed the difference in SFRs to the lack of feedback included in our subgrid model. We have shown previously that the accretion history of a clump can have a significant impact its SFR and feedback, especially radiative feedback, can greatly alter the accretion (Dale et al., 2007; Peters et al., 2010; Bate, 2012; Dale et al., 2012; Klassen et al., 2012; Kim et al., 2012). On smaller scales, the inclusion of radiative feedback suppresses fragmentation by increasing the temperature locally. On larger scales, ionizing radiation can clear gas from the clump by driving large scale outflows. These mechanisms tend to decrease the accretion rate and the SFR. When our model is included in full hydrodynamical simulations which include radiative feedback, the accretion will be determined self-consistently rather than specified beforehand. The full simulations should therefore show better agreement with the measurements by Lada et al. (2010a).

The characteristic timescale τ_{SFR} for star formation is by definition $\tau_{SFR} = M/(SFR) \sim M^{1-\alpha}$. The actual model numbers from the different panels in Fig. 8 fall in the range $\simeq 3$ Myr within factors of two. Since $3t_{ff} \sim 1$ Myr in our simulations, our results should provide in principle provide a useful prediction for the expected *age range* within a young, relatively massive star cluster: they should take only a few Myr to build. Direct observational comparisons with such objects nearby are made more difficult by the inevitable presence of dust and differential extinction within actively star-forming clusters, but an age range at the 3-Myr level seems comfortably realistic. One example is the massive ($> 2 \times 10^4 M_{\odot}$) cluster R136 in 30 Doradus, for which a recent study (Andersen et al., 2009) finds a mean age of 3 Myr

and an internal age spread of nearly the same amount (Massey & Hunter, 1998). A very similar set of conclusions has been suggested for the massive young cluster at the centre of NGC 3603 (Melena et al., 2008; Pang et al., 2013), in which an age range of a few Myr may show up for the lower-mass stars particularly.

One of the most important properties of a cluster in terms of its radiative feedback is the number of O stars that are formed. In this work, an O star is defined to be any star whose mass exceeds $16 M_{\odot}$. Since a single O star can have a luminosity greater than $10^5 L_{\odot}$ (Carroll & Ostlie, 1996) and have most of its energy output in the form of UV photons, under or over-producing O stars can significantly alter how the cluster interacts with its surroundings. It is therefore important to verify that our model is reproducing the expected number of O stars. Directly integrating the IMF results in approximately 0.28 % of the stars formed having masses greater than $16 M_{\odot}$. In Figure 3.10, we have plotted the percentage of stars which are O stars. As in Figure 3.6, the points represent the average value and the error bars are one standard deviation. It can be seen from this figure that the highest mass cases agree with the expected value.

Figure 3.10 shows that the lowest mass model which produces O stars has a final clump mass of $5000 M_{\odot}$ which gives a rough threshold for the emergence of massive stars. Interestingly, the present day mass of the ONC is roughly $4800 M_{\odot}$ (Hillenbrand & Hartmann, 1998) and also contains a small number of massive stars (~ 5 stars greater than $16 M_{\odot}$ from Hillenbrand (1997)) suggesting that our model is behaving as expected. The model with an accretion rate of $1000 M_{\odot} t_{ff}^{-1}$ seems to be underproducing O stars in the cases of low initial clump mass compared to what

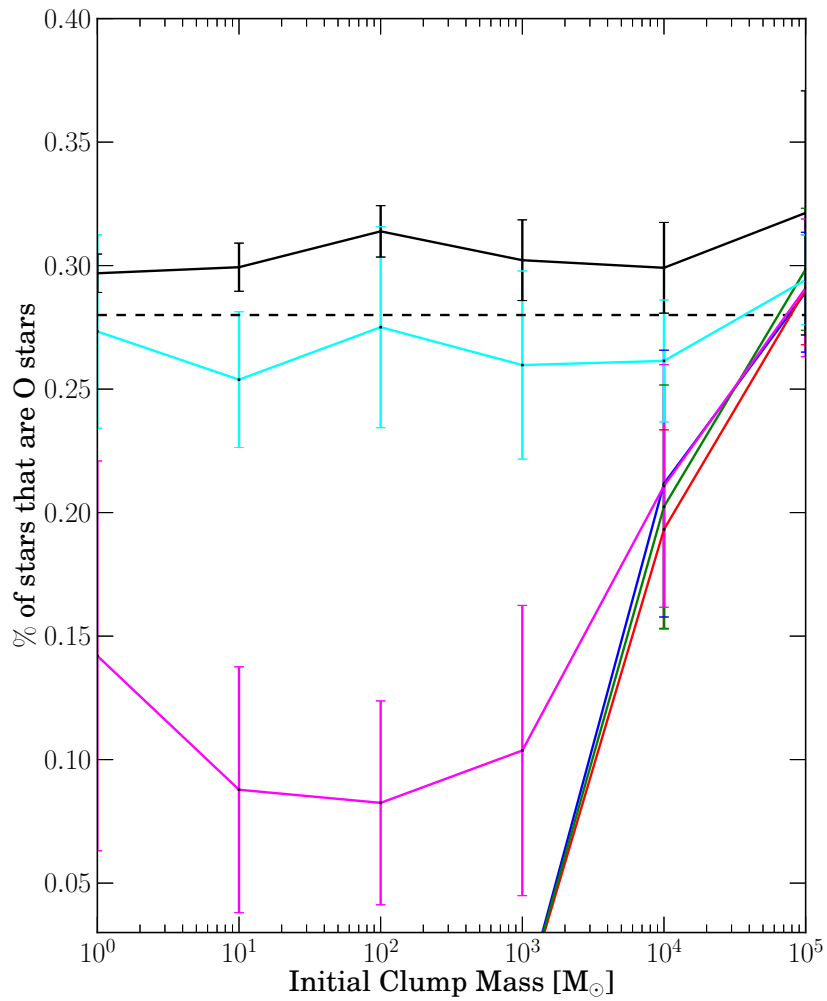


Figure 3.10: The percentage of O stars formed from the models shown in Figure 3.6. As discussed in the text, the expected percentage of O star from directly integrating the IMF is 0.28%. The points represent the average of all runs and the error bars represent one standard deviation. The colour coding is the same as in Figure 3.6.

is expected directly from the IMF. Work by Williams & McKee (1997) suggests that roughly 50% of clouds with a mass of $10^5 M_{\odot}$ should form at least one O star which is consistent with our results. This, together with the number of ionizing photons from Figure 3.2, suggests that our model is working as expected.

There are a few caveats to our model. The expected percentage of O stars mentioned earlier assumes that the IMF is fully sampled which may not be the case if there is insufficient mass to form massive stars. Also, the clumps in our model are still actively accreting gas after 5 freefall times so star formation is still ongoing and massive stars still have a probability of forming. This can be seen in Figure 3.3 from the large reservoir masses and in Figure 3.2 from the non zero SFRs at the end of the simulation. The imposed condition of constant accretion onto the clump is also artificial. The actual accretion rate could be higher as suggested in Murray & Chang (2012). A higher accretion rate would lead to a building up of the reservoir mass leading to a higher chance of forming an O star.

3.6 Summary and Conclusions

We have presented a model with the aim of being used in hydrodynamical simulations to represent the radiative output of an entire star cluster. The model starts with a clump of a specified mass and forms main sequence stars by sampling the Chabrier IMF. Every tenth of a freefall time, or 3.6×10^4 years assuming a density threshold of 10^4 cm^{-3} for cluster formation, a fraction of the remaining gas inside the

cluster is converted to stars. We have shown that sampling every tenth of a freefall time reproduces the correct number of high and low mass stars.

To test our model, we ran multiple simulations by varying the initial clump size and accretion rate. We have shown the following:

- The model we have presented is a straightforward way to determine the radiative output of clusters ranging in size from small subclusters of $\sim 10 M_{\odot}$ to the globular cluster regime ($\sim 5 \times 10^5 M_{\odot}$) with varying accretion rates.
- How a clump gets its mass has an impact on its properties. There are two different regimes we have identified; 'accretion' dominated, and 'reservoir' dominated. The accretion dominated regime is characterized by an increasing SFR and a less sampled IMF due to the smaller number of stars formed. The reservoir dominated regime has all mass present in an initial clump and is characterized by a decreasing SFR and a more fully sampled IMF. Differences between the two regimes disappear with a sufficiently large clump mass.
- We have shown that typical clump accretion rate can produce a fully sampled IMF regardless of the initial clump mass at the onset of star formation.
- Our model reproduces the number of ionizing photons released from a cluster from previous, more detailed simulations. For a clump size on the order of $10^4 M_{\odot}$ the resulting ionizing photon rate is between $10^{50-51} \text{ s}^{-1}$. For high mass clusters, this is expected because the IMF is fully sampled.

- Our model can reproduce the range in SFRs observed in nearby molecular clouds (10^{-5} - $10^{-2} M_{\odot} \text{ yr}^{-1}$) and reproduces the observed SFR for similarly sized star forming regions. We find that small ($\sim 100 M_{\odot}$) clusters have SFRs of 10^{-4} - $10^{-5} M_{\odot} \text{ yr}^{-1}$ while larger clusters ($> 10^4 M_{\odot}$) can exceed $10^{-2} M_{\odot} \text{ yr}^{-1}$. Lower mass clusters also exhibit more variability in their SFRs than higher mass clusters.
- The SFR is nearly proportional to clump mass at all times $\leq 4 t_{ff}$. This agrees with multiple observations of star forming clump on both large and small scales (Gao & Solomon, 2004; Wu et al., 2005; Lada et al., 2010b,a).
- We find a timescale for star formation of roughly 3 Myrs which provides a useful prediction for the expected age range within a young, relatively massive star cluster. This timescale is consistent with observations of R136 (Andersen et al., 2009).
- High mass clusters ($> 10^4 M_{\odot}$) produce the correct number of O stars expected from the IMF. We have identified a final clump mass threshold for O star formation of $\sim 5000 M_{\odot}$ which consistent with observations of 5 stars with masses greater than $16 M_{\odot}$ in the ONC (Hillenbrand, 1997) which has a present day mass of $\sim 4800 M_{\odot}$.

This paper will followed by results of cluster formation simulations using the AMR code FLASH.

Chapter 4

Numerical Methods

The subgrid model introduced in the previous chapter was included into the code FLASH in order to run full hydrodynamical simulations with radiative transfer. The first part of the current chapter is dedicated to outlining several aspects of the FLASH code. This includes an introduction to adaptive-mesh refinement, sink particles, and the hybrid characteristics raytracing method used to treat radiative transfer. The second part of this chapter outlines the modifications made to the FLASH code to include the subgrid model for cluster formation.

4.1 FLASH Code

The FLASH code is a modular, adaptive-mesh, simulation code designed to handle general compressible flow problems found in a wide range of astrophysical environments (Fryxell et al., 2000). It solves the hydrodynamics equations on an adaptive Eulerian mesh and is designed to run in parallel using the Message-Passing Interface (MPI) library. Adaptive mesh refinement, or AMR, (Berger & Colella, 1989) is a

technique used to greatly increase the computational speed and memory efficiency of grid based codes. It works by selectively increasing the resolution in regions where it is needed, such as areas of high density, while leaving less dynamically important regions at a lower resolution.

As mentioned above, FLASH can be used to model a wide range of astrophysical situations on small and large scales. Some examples of its uses so far are modeling protostellar disks (Banerjee et al., 2004; Seifried et al., 2013), protostellar jets (Banerjee & Pudritz, 2006, 2007), collapse of turbulent molecular clouds (Federrath et al., 2010), ambipolar diffusion in star formation (Duffin & Pudritz, 2008), supernova events (Dubey et al., 2008), and the large-scale evolution of galaxy clusters (Ricker et al., 2001).

There are several modules available in the 2.5 version of the code that are used in this work. These include hydrodynamical and gravity solvers, heating and cooling due to dust and molecules, a radiative transfer routine developed by Peters et al. (2010), and Lagrangian sinks particles developed by Federrath et al. (2010) and used extensively in Dr. Pudritz's research group.

4.2 Sink (and Cluster) Particles

Simulations of star formation in molecular clouds must be able to follow the evolution of both the diffuse component of the ISM, and the runaway collapse of overdense regions which eventually form stars. This large density range leads to a fundamental numerical issue related to the Truelove criterion which states that the Jeans length

of a collapsing region must be resolved by at least 4 grid cells to avoid spurious numerical fragmentation (Truelove et al., 1997; Bate & Burkert, 1997). However, the Jeans length scales as $\lambda_J \propto \rho^{-1/2}$ meaning that more resolution is required as the collapsing region gets more dense in order to satisfy the Truelove criterion. The resolution cannot be increased indefinitely since there is both a maximum resolution and memory limits so an alternative approach is needed.

This issue is compounded with a decreasing timestep as the density increases. FLASH does not have adaptive timestepping (i.e. different timesteps for different regions of the grid) so the global timestep is determined by the region of the computational volume with the shortest dynamical time. As with the Jeans length, the dynamical time, or free-fall time, scales as $t_{ff} \propto \rho^{1/2}$ meaning that a single dense and collapsing region can cause the simulation to grind to halt.

The solution to this issue is the use of sink particles. These are a computational tool which replaces an area of high density gas that meets a certain set of criteria with a particle of equal mass. The particle is Lagrangian, meaning it moves independent of the grid, and can still interact gravitationally with its surroundings while accreting gas. The sink particle prescription we use was developed by Federrath et al. (2010) and contains the following checks before creating a particle;

- Above a certain density threshold,
- Must be on the highest level of refinement,
- The gas is converging in three dimensions,

- There is a central gravitational minimum,
- The region is Jeans-unstable,
- Gravitationally bound,
- Not within the accretion radius of another particle

These checks ensure that spurious particle formation does not occur during transient events such as shocks which has been an issue in previous implementations (Federath et al., 2010).

To adapt the sink particles to be used as cluster particles, several particle properties had to be added for this work. The added properties are;

1. Total mass of stars inside cluster particle
2. Number of stars inside the cluster particle
3. Total output luminosity
4. Non-ionizing luminosity
5. Time of last IMF sampling (used to determine when to form new stars).

4.3 Radiative transfer methods

The implementation of a radiative transfer routine into star formation simulations is vital. As discussed earlier, the radiative output of stars and clusters is responsible for heating and ionizing the surrounding gas which is responsible for suppressing

fragmentation, stopping accretion onto forming stars, and dispersing the remaining gas. Radiative transfer routines have been implemented by several authors in studies of star formation (Whitehouse et al., 2005; Commerçon et al., 2010; Bate, 2012; Seifried et al., 2013) and follow one of two main approaches. Each of these approaches operate within a limited region of opacity and are not solutions to the complete radiative transfer problem.

The first main approach to treating radiative transfer is flux-limited diffusion (FLD). This approach assumes the radiation field can be well approximated by the mean radiation intensity (Minerbo, 1978; Levermore & Pomraning, 1981),

$$J_\nu(r) = \frac{1}{4\pi} \int_{\Omega} I_\nu(r, \Omega) d\Omega, \quad (4.1)$$

which reduces the dimensionality of the problem from 6 to 4. The radiation is tightly coupled with the matter and diffuses like a fluid through the gas. This assumption, however, is only valid in regions of high optical depth and breaks down in transition regions such as the atmospheres of protoplanetary disks (Nordlund, 2011). FLD also is only concerned with the space angle dependence of the radiation field since the frequency dependence greatly increases the numerical complexity.

The second main approach, and the one used in the work, is called raytracing. This method works by casting 'virtual' rays from the source to all cells in the computational domain in order to calculate the amount of energy, corrected for the obscuration of the intervening material, deposited in each cell. This technique is not as accurate as FLD in high optical depth regions but has the advantage of casting

shadows and is easily expandable to multifrequency treatments of radiative transfer. Raytracing schemes are simplified by ignoring any scattering events or reemission events after energy is absorbed. This means that the intensity due to a source can be expressed simply as,

$$I(r) = I_s(0)e^{-\tau(r-r_s)} \quad (4.2)$$

where $I_s(0)$ is the intensity of the source and τ is the optical depth between the source and the region of interest. The total intensity at a point is then just a sum over all emitting sources.

There are two main implementations of raytracing in hydrodynamical simulations. The first is the “long characteristics” method in which a ray is drawn from the source cell to each cell in the computational domain. This approach is beneficial because it is accurate and easily parallelizable but is computationally expensive because many rays pass through the through the cells closest to the source. This results in redundant calculations of column density. The contrasting approach is called “short characteristics” and works by drawing rays along cell edges starting from the source cell. To get the total column density between the target and source cell, the column density of each ray is added together. Because of this, the short characteristics method cannot be parallelized since the column density calculation has to be done in a specific order and the contributions from all cells between the target and the source must be known beforehand. See Figure 4.1 for a visual representation of the short and long characteristics methods.

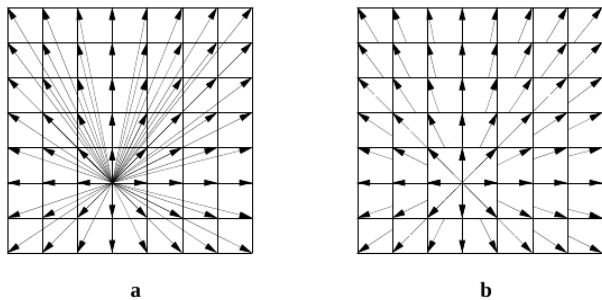


Figure 4.1: A comparison between long characteristics (left) and short characteristics (right) raytracing from Rijkhorst et al. (2006). In the long characteristics method, a ray is drawn from the source to all cells resulting in redundant calculations shown by multiple rays passing through the same cells. The short characteristics method avoids this redundancy but is inherently serial.

It should be noted that there are more complete methods available to study the complete radiative transfer problem. The first of these is through Monte Carlo codes which use probabilistic methods to simulate the random walk of a photon through a medium. This is a computationally expensive method, however, because it requires the passage of a large number of photons for the results to converge. This makes the method inapplicable to large computational volumes with many sources. A recent advance is the hybridization of raytracing and FLD method by Kuiper et al. (2012). A raytracing scheme is used initially to deposit energy into cells which then diffuses throughout the surrounding gas via FLD. This promising method is being generalized for turbulent star formation (Klassen & Pudritz, in prep.).

4.3.1 Radiative transfer in FLASH

The raytracing approach used in FLASH, developed by Rijkhorst et al. (2006), is a hybridization of the above two approaches and is appropriately deemed “hybrid characteristics”. It avoids redundant calculations while still being parallelizable. The FLASH computational domain is divided into “blocks” which contain 8x8x8 cells with guard cells surrounding the blocks. The guard cells are used to calculate derivatives of quantities around block boundaries and also surround the entire computational volume. The fluid properties in the guard cells are either determined by neighbouring blocks or a user-specified external boundary condition. The code is parallelized by distributing the blocks to separate processors. The long characteristics method is then used to calculate radiative transfer within an individual block while the short characteristics method is used for rays which cross between blocks. Using long characteristic raytracing within blocks significantly reduces the number of redundant calculations. The column density is also calculated independently in each block meaning that the total column density between the source and the target cell can be easily found by summing the contributions from intervening blocks. For a more detailed description of the hybrid characteristics code, see Rijkhorst et al. (2006).

4.4 Heating and Ionization in FLASH

The raytracing routine described above is coupled with a package (the DORIC package) which handles heating, cooling, and ionization in the gas. The total amount

of ionization is found by balancing the ionization rates due to photoionization and collisional ionization with the electron recombination rate. The number of ionizations per second due to photoionization is given by (Osterbrock, 1989),

$$A_p = \int_{\nu_0}^{\infty} \frac{4\pi J_\nu}{h\nu} \alpha_0 d\nu \quad (4.3)$$

where ν_0 is the threshold energy for hydrogen ionization (13.6 eV), α_0 is the ionization cross-section of hydrogen, and J_ν is the mean intensity of radiation. It should be noted that a 'grey atmosphere' approximation is used to represent the ionization cross-section, meaning that it does not have any frequency dependence. The mean intensity of the radiation is given by,

$$J_\nu(\mathbf{r}) = \left(\frac{R}{|\mathbf{r}|} \right)^2 \frac{2\pi}{2c^2} \frac{h\nu^3}{\exp(\frac{h\nu}{kT}) - 1} \exp(-\tau(\mathbf{r})) \quad (4.4)$$

where R , T , and $\tau(\mathbf{r})$ are the source's radius, the source's temperature, and the optical depth a distance \mathbf{r} from the source, respectively. In the case of stellar sources, the radius and temperature are found by assuming blackbody sources with temperatures equal to the effective temperature and the surface of the star.

The contribution to the ionization rate due to collisions is given by,

$$A_c = A_c(\text{HI}) n_e \sqrt{T} \exp(-I(\text{HI})/kT) \quad (4.5)$$

where $I(HI)$ is the hydrogen ionization potential (Cox, 1970) and $A_c(HI)$ is a constant.

Electron recombination is given by,

$$\alpha_R = \alpha_R(10^4\text{K}) \left(\frac{T}{10^4} \right)^{-0.7} \quad (4.6)$$

where $\alpha_R(10^4\text{K}) = 2.59 \times 10^{-13} \text{ cm}^3\text{s}^{-1}$.

There are two ways to heat the gas; heating due to photoionization, and heating due to non ionizing radiation. The heating rate due to photoionization is given by

$$\Gamma_p = n(\text{HII}) \int_{\nu_0}^{\infty} \frac{4\pi J_\nu}{h\nu} a_0 h(\nu - \nu_0) d\nu \quad (4.7)$$

where $n(\text{HII})$ is the number density of ionized hydrogen. The heating due to non-ionizing radiation is simply the luminosity of the source modulated by the intervening column density.

The gas is also cooled via cooling curves taken from Dalgarno & McCray (1972) which assume solar metallicity.

4.5 Adding cluster particles to raytracing

4.5.1 Populating the cluster with stars After a sink particle forms, it needs to be populated with constituent stars. The model we are using to populate the cluster

has been described in detail in the previous chapter but a brief discussion about how this has been implemented in FLASH is required. All changes have been made directly to the raytracing routine to keep the code localized. Each sink particle has a corresponding array which records the masses of all stars that have formed within it and the time at which they formed. This allows the stellar mass function of each cluster to be tracked over time.

Before raytracing takes place, the time since the last sampling is determined for each particle. If this time is less than a tenth of a freefall time (see Chapter 3) then no sampling takes place and the particle properties are not updated. If it has been longer than a tenth of a freefall time since the last sampling, then new stars are formed via the model described earlier. The masses of the new stars formed are then recorded and passed to the routines handling ionization and heating of the gas. The sampling is done on a single processor only, The added particle properties, given in section 4.2, are then updated accordingly.

It is important to note that the sampling is done on a single processor only due to the stochastic nature of the model. If this was not the case then the stellar mass functions in a sink particle would not agree between processors. The sampling of the IMF is therefore done on a single processor and the results are communicated between processors afterwards.

There is a significant difference between sink particles and cluster particles that needs to be mentioned. As described in Chapter 2, cluster merging events are significantly more common than stellar mergers so we have included this capability into

cluster particles. There are two conditions which determine whether two cluster particles will merge. First, the two particles must be within the accretion radius of each other which is set to be 4 grid cells on the highest level of refinement surrounding the particle. Second, the particles must be approaching each other and bound meaning they do not have enough kinetic energy to reach a greater distance apart than the accretion radius. If these conditions are met, the smaller particle is merged to the larger one. All properties of the smaller particle are added to the larger one including the newly added cluster particle properties described earlier (except the time of last sampling which is unaffected by the merger).

4.5.2 Heating and ionization due to cluster particles The major difference in using sink particles for clusters is that the ionization and heating are due to a collection of stars. The calculation of these quantities is simplified by recording the mass of all its stellar constituents. The total ionization and heating rates are just the sum of the rates from the constituent stars. To perform the sum, however, the temperatures and radii of the cluster stars need to be known since the mean intensity appears in both quantities. We use the analytic functions given in Tout et al. (1996) to determine the stellar radius and effective temperature of each star from its mass. The procedure for calculating the total photoionization and photoionization heating rates goes as follows. For every star present in the cluster particle, the radius and temperature are found via the analytic functions. These are used to calculate the individual stellar photoionization/heating rates and added to a running total. After the calculation, the totals are saved and passed to the raytracing routine. This

procedure is repeated for every cluster particle in the computational volume. If no new stars are formed in the next timestep, then the saved values are again passed to the raytracing routine. If new stars are formed, the contributions due to the new stars are added to the running total and are saved for future use.

The heating due to non-ionizing radiation requires the non-ionizing luminosity of the cluster to be known. Again, this is just the sum of the non-ionizing luminosity of its member stars. A lookup table with 300 entries for the non-ionizing luminosity of stars with masses between 0.1 and 100 M_{\odot} was created in order to increase the code's efficiency. The total non-ionizing luminosity is found by looping over all stars in a cluster particle, finding the nearest mass entry in the table, and adding the corresponding luminosity to the running total. As with the photoionization/heating rates, the non-ionizing luminosity is calculated once and saved until new stars are formed at which point their contributions are added to the previous total.

The DORIC routines also include heating due to accretion luminosity from individual stars. The accretion luminosity can contribute significantly to the total luminosity during the prestellar phase especially during episodic accretion events (Offner & McKee, 2011). In this work, however, we have chosen to ignore the effects of accretion luminosity. The main reason for this is that it requires knowledge about the accretion rate onto the stars inside the cluster particle. Our model assumes that all accreted mass is used to form main sequence stars meaning there is no accretion onto stars after they form. If this was not the case, we would have to introduce further parameters into our model which describe what fraction of accreted mass is used to form new stars versus being accreted onto already formed

stars. Moreover, protostellar accretion rates have a dependence on mass which introduces another complication (Schmeja & Klessen, 2004; Krumholz et al., 2006c). Since these parameters are currently not well constrained, we ignore the effects of accretion luminosity in this work.

To justify the absence of accretion luminosity, we can consider the timescale for massive star formation. Since massive stars are the largest contributors to the overall cluster luminosity, an increased luminosity of these stars during the prestellar phase will likely have a significant impact. McKee & Tan (2003b) have shown that it takes $\sim 10^5$ yrs for a massive star to reach the main sequence. Considering the freefall time presented in Chapter 3 was 3.65×10^5 yrs and models were run for 2 Myrs, the overall impact of prestellar evolution would likely play a minor role. While the luminosity during the prestellar phase is higher compared to the main sequence phase, the difference is no larger than an order of magnitude (McKee & Tan, 2003b) again suggesting it is appropriate to ignore accretion luminosity and prestellar evolution. Nonetheless, our estimates for total cluster luminosity represent minimum values.

Our model discussed in Chapter 3 can be augmented slightly to include the effects of prestellar evolution. This would involve randomly selecting a *final* stellar mass and setting aside that mass. The star's evolution would then follow a pre-main sequence track, like those in Hosokawa & Omukai (2009), for a chosen amount of time before reaching the main sequence. Since fiducial values for the accretion rate are built into these prestellar models, we would not need to add individual stellar accretion rates ad hoc.

Chapter 5

Simulation Results

The current chapter will outline the results of three hydrodynamical simulations performed using FLASH which incorporated the cluster particle model described in Chapter 3. Identical simulations with and without radiative transfer allow the effects of radiative feedback to be examined. The resulting cluster particle properties are discussed and the cluster mass distribution also compared to observations.

5.1 Initial conditions Three simulations have been run to compare the effects of increased resolution and the inclusion of radiation. All simulations have the same initial conditions. The simulated region is 11 pc in size and contains a total of $5.8 \times 10^4 M_{\odot}$. The initial density profile is peaked at the centre with a density of 6500 cm^{-3} and radially decreases outwards as $r^{-3/2}$. The peak density was chosen deliberately to be less than the cluster formation threshold of 10^4 cm^{-3} to allow some time for the region to collapse before forming clusters. Rigid body rotation around the z-axis, with an angular velocity of $1.1 \times 10^{-14} \text{ s}^{-1}$, is included. This is added to reproduce the non-zero angular momentum observed in molecular clouds.

Table 5.1: Summary of simulation parameters and results

Name	Radiation	Total Mass [M_{\odot}]	Resolution [pc]	Number of Sinks	Simulation Time [Myr]
RHD6	Yes	5.80×10^4	0.04	95	1.11
HD6	No	5.80×10^4	0.04	5	1.94
HD8	No	5.80×10^4	0.01	1	0.17

An initial supersonic turbulent velocity field with no further driving is also included. A Burger’s spectrum (ie. the power at different wavenumbers, k , varies as k^{-2}) with a Mach number of 4 is used. The initial temperature is set to 10 K everywhere in the volume,

The three simulations are denoted as RHD6, HD6, and HD8 where R indicates radiative feedback is present, HD stands for hydrodynamics, and the number indicates the maximum refinement level in the simulation. A maximum refinement level of 6 and 8 translate to a resolution of 0.04 pc and 0.01 pc, respectively. See Table 5.1 for a summary of the simulation properties.

5.2 Radiative feedback effects

Figures 5.1 and 5.2 show a slice through the middle of the z -axis at 0.15, 0.5, 0.75, and 1 Myrs for runs RHD6 (Figure 5.1) and HD6 (Figure 5.2). The locations of the cluster particles have been projected onto this slice. It can be seen that both runs start similarly with turbulence breaking up the gas and one cluster particle forming in the center. There are significant differences however that arise later, as seen in the bottom rows of Figure 5.1. At 1 Myr, RHD6 has produced 44 cluster sink particles

while HD6 has produced only 3. The large number of cluster particles in RHD6 are grouped within the inner 2 pc of the simulation.

The early evolution of both simulations is similar. The turbulence initially breaks the gas into a network of small and intersecting filaments. One large particle forms immediately in the high density region in the center of the simulation and reaches a mass of $750 M_{\odot}$ by 0.15 Myrs. As the simulations evolve, the number of filaments decreases but the ones that remain are wider and more well defined. These filaments branch off the central overdense region and are likely providing mass to the accreting cluster particles. By 1 Myr, there are three well defined filaments which intersect at the center of the computational volume.

Only one particle forms in the first 0.4 Myrs of both RHD6 and HD6. At 1 Myr, run HD6 has formed three particles with masses of 79.4, 4.96×10^3 , and $2.16 \times 10^4 M_{\odot}$. Run RHD6 is dominated by two particles of masses $6.96 \times 10^3 M_{\odot}$ and $120 M_{\odot}$ until a time of ~ 1 Myrs at which point a large number of clusters particles form in the central region. A total of 47 cluster particles have formed in run RHD6 by 1 Myr.

The emergence of the large number of particles is due to likely due to a spiral wave triggered by the close interaction of cluster particles in the central region. Figure 5.3 shows the density in the x-y plane just before and after the burst of cluster particle formation at times of 0.93, 0.95, 0.97 and 0.99 Myrs. The interaction between a few particles produces a high density region which rotates around the centre. This high density region then quickly fragments leading to a large number of cluster particles

being formed in a small volume. There is no such close interaction in HD6 between cluster particles, so the same behaviour is not seen.

Radiative feedback from the cluster particles in RHD6 has a dramatic effect on the temperature structure and dynamics of the gas. The gas surrounding the grouping of particles is heated to $\sim 2 \times 10^4$ K. The heating is also capable of driving large scale outflows, as seen in Figures 5.4 and 5.5 which show the inner region of the computational domain. The rows corresponds to times of 0.93, 0.94, 0.97, and 1.1 Myr from top to bottom. Velocity vectors are overplotted to show the direction of the flow. It can be seen from these figures that a large scale outflow is driven by the group of clusters at the center. Unlike HII regions however, the inside of this outflow does not remain at $\sim 10^4$ K but cools quickly to 10 K (the minimum allowable temperature in our simulations). There is also very little ionization inside the outflow.

We propose that this is due to similar effect that is seen by Klassen et al. (2012). In their simulations, a series of bursts are observed which drive outflows. These are attributed to the building up of pressure due to ionizing radiation which is confined by the infalling gas. Eventually, the pressure becomes strong enough to break through the accreting gas resulting in a burst. A similar mechanism could be at work here where the extreme heating in the vicinity of the clusters increases the pressure of the gas which results in an outflow. The expanding outflow then cools rapidly except at the expanding front which is kept at high temperatures due to shock heating. The corresponding density plots show the outflow is launched towards a region of low density. This is similar to the behaviour seen in Dale et al. (2012) who showed that heating and ionizing radiation is preferentially released in the direction of low density voids perpendicular to filaments.

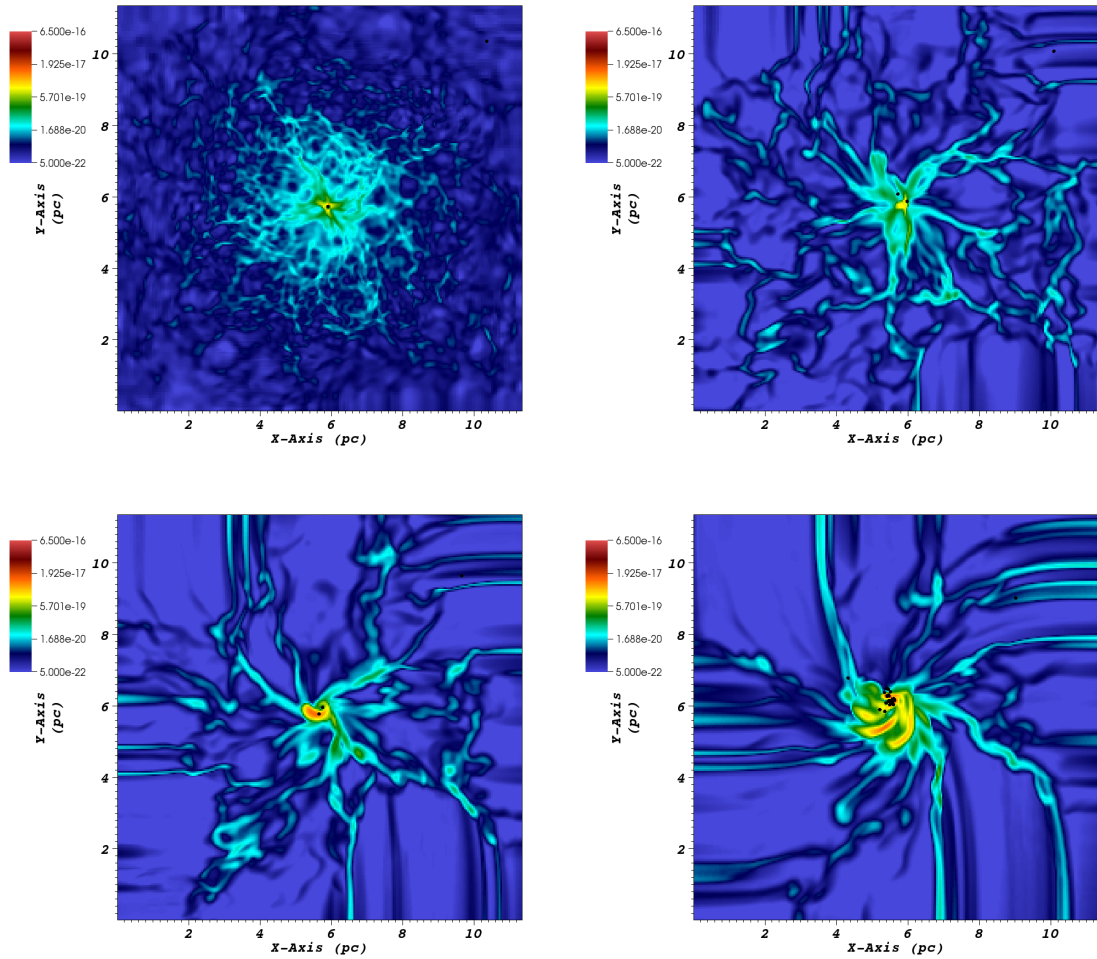


Figure 5.1: A density slice (in g cm^{-3}) showing a slice through the center of the z-axis for run RHD6. The locations of the cluster particles are projected onto this slice and shown by the black dots. The plots represent times of 0.15, 0.5, 0.75, and 1 Myrs from top to bottom and left to right.

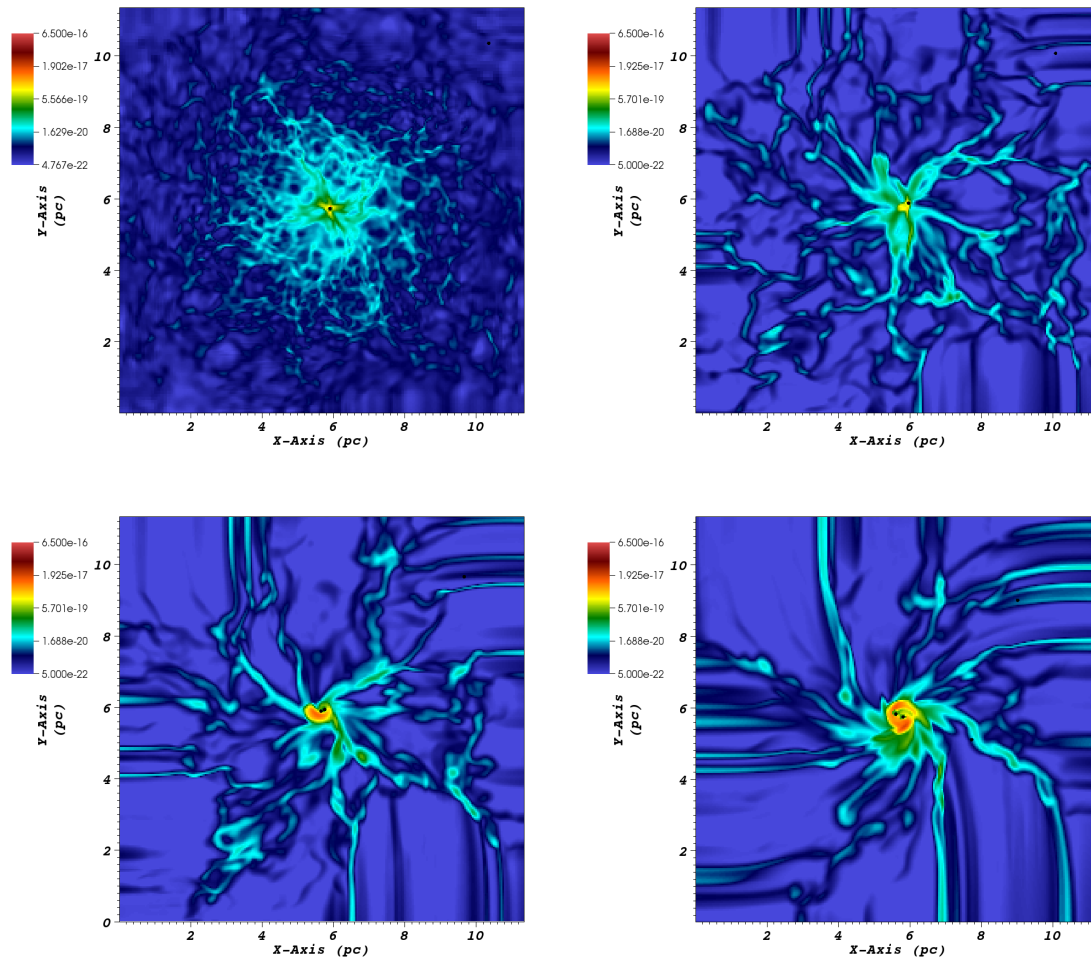


Figure 5.2: A density slice (in g cm^{-3}) showing a slice through the center of the z-axis for run HD6. The locations of the cluster particles are projected onto this slice and shown by the black dots. The plots represent times of 0.15, 0.5, 0.75, and 1 Myrs from top to bottom and left to right.

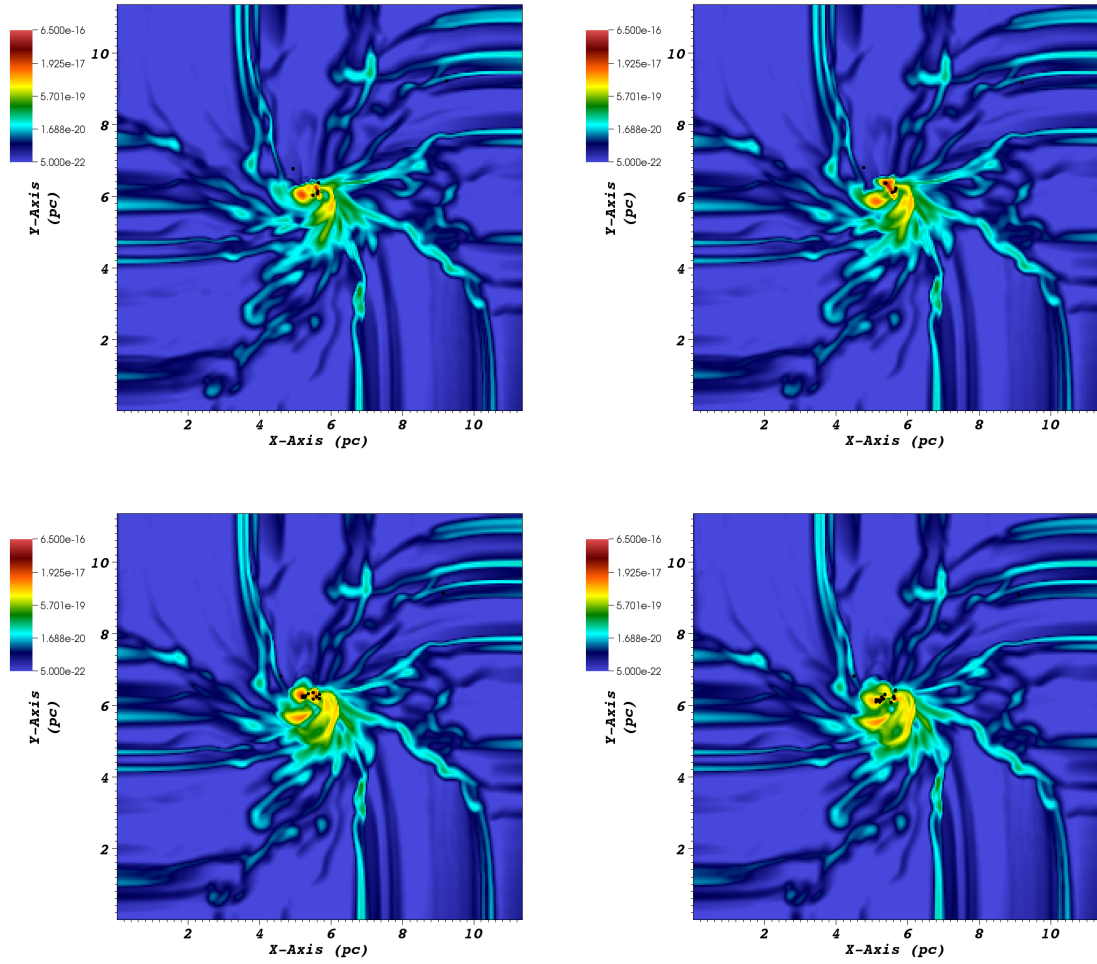


Figure 5.3: Density slices (in g cm^{-3}) along the z-axis showing the emergence of a large number of cluster particles in RHD6. Interactions between cluster particles produces an overdense region which rapidly fragments to form new particles. The plots are shown at times of 0.93, 0.95, 0.97, and 0.99 Myrs.

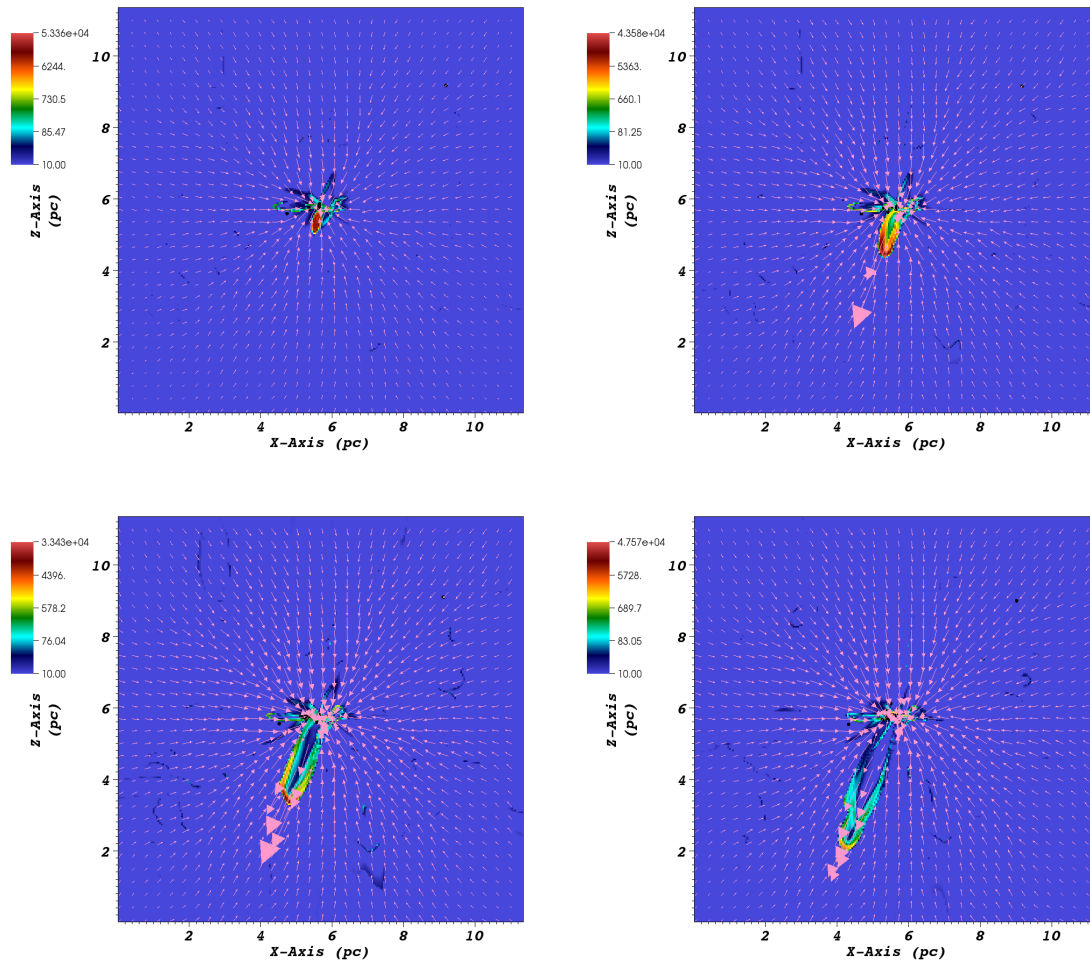


Figure 5.4: Temperature slices (in Kelvins) through the x-axis showing a side on view of an outflow emerging from a group of particles clustered near the center of the computational volume in RHD6. The arrows show the velocity of the gas, indicating that the loop structure is indeed an outflow.

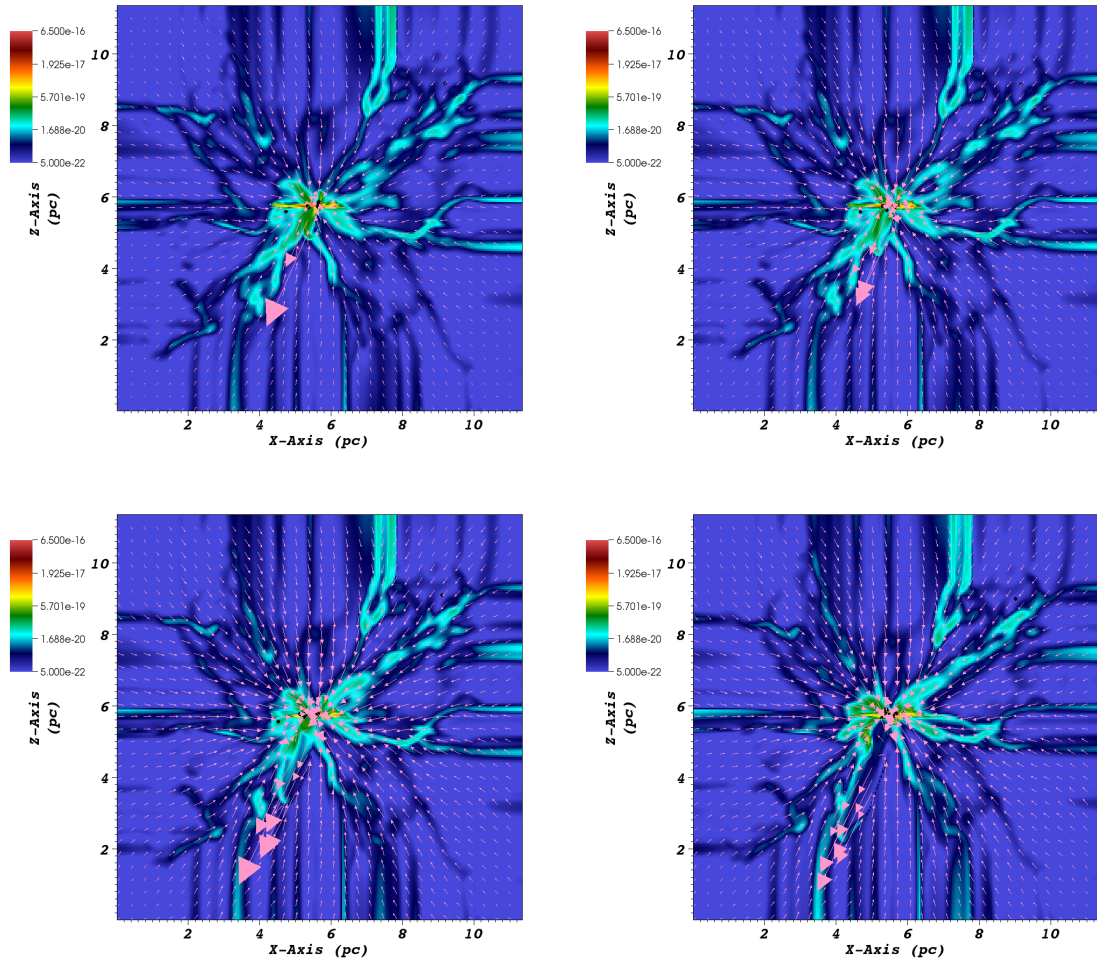


Figure 5.5: The density corresponding to the plots shown in Figure 5.4. The outflow is launched into a region of low density and is confined by a filament on one side.

The presence of outflows presents another possibility for the emergence of particles at ~ 1 Myr. Their formation may have been triggered by the outflow. The outflow shown in Figures 5.4 and 5.5 starts at 0.93 Myrs, consistent with the formation of clusters in the centre of the volume. Triggering of star formation has been observed in other simulations which include feedback (Dale et al., 2005, 2007, 2012) so we may be seeing a similar effect.

To further quantify the differences between runs, we have plotted the mass of all cluster particles as a function of time in Figure 5.6 for RHD6, HD6, and HD8. Due to constraints on computational resource time, HD8 could only be run for ~ 175 kyr. While there is only one particle in the simulations at this time, there is no significant difference in particle mass between runs. This suggests that numerical convergence is not a significant issue in this work but HD8 will need to be evolved further for this claim to be verified.

Figure 5.6 clearly shows that radiative feedback is affecting the accretion onto cluster particles. The particles in run RHD6 accrete for a significantly shorter time than those in HD6. This is seen most clearly in the mass evolution of the first particle that forms. The particle grows identically in mass between runs until ~ 0.4 Myr at which point the accretion stops completely in RHD6. Particles that form later in RHD6 stop accreting almost instantly after they form. This behaviour is not seen in run HD6. The radiation being produced in RHD6 is clearly heating and dispersing the gas enough to strongly reduce accretion.

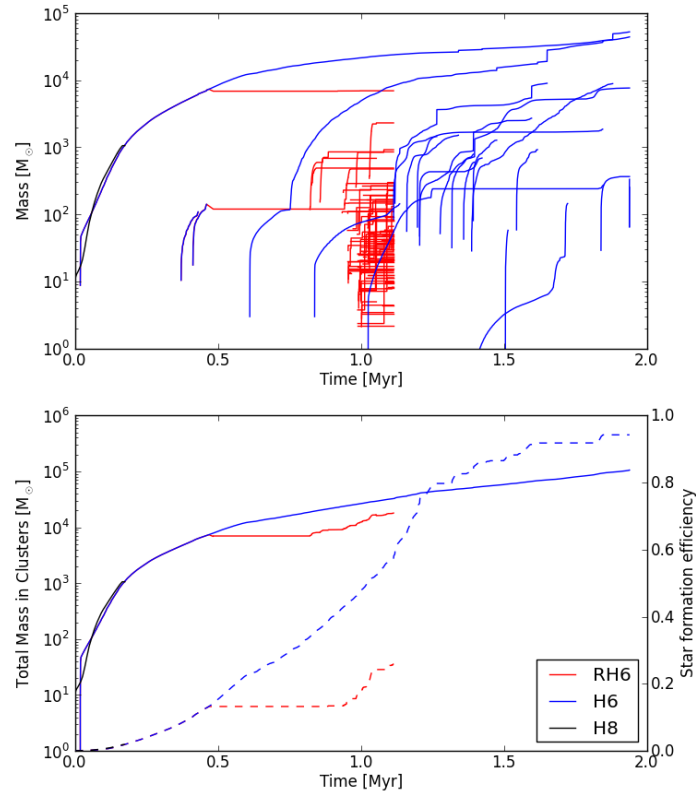


Figure 5.6: **Top:** A plot showing the mass of all cluster particles that form in the three simulations as a function of time. RH6, HD6, and HD8 are coloured red, blue, and black, respectively. Lines that end abruptly are either due to the simulation ending or merger events. **Bottom:** The total mass present in cluster particles as a function of time and the respective star formation efficiency. The total mass in clusters is given by the solid lines and the star formation efficiency by the dashed lines. Note that the star formation efficiency is defined as the total mass in clusters divided by the instantaneous mass in the simulation to account for mass growth. Clearly, radiative feedback is strongly suppressing the formation of clusters.

The emergence of a large number of small mass particles in RHD6 around 1 Myr seems to go against previous simulations which have shown that radiative feedback prevents the fragmentation of gas. While the emergence of these particles is likely due to a passing spiral wave, we could be seeing a similar effect as seen in Parker & Dale (2013). These simulations showed that simulations which include radiative feedback tend to produce clusters that are more subclustered and remain subclustered for a longer period of time. Since the particles that emerge at 1 Myr are tightly grouped together, we could be seeing the same effect in our work. Due to the close proximity of these particles, we expect that merging will decrease the number of particles over time.

Even though a larger number of particles appears in run RHD6 compared to HD6, radiative feedback still suppresses the large scale fragmentation of the cloud. This can be seen in the bottom panel of Figure 5.6, where we have plotted the total mass in sinks (solid lines) and the corresponding star formation efficiency (dashed lines) defined as,

$$\epsilon_{SF} = \frac{M_{sinks}}{M_{total}} \quad (5.1)$$

where M_{sinks} is the total mass contained in cluster particles and M_{total} is the total mass in the simulation.

There is an important note to make here about the total mass in the simulation. When analyzing the simulation results, it was noticed that the total mass in the simulation volume was growing despite having outflow conditions at the boundary.

The mass in HD6 doubled by the end of the simulation and the mass in RHD6 grew by $\sim 20\%$. We have attributed this to mass being drawn in from the ghost cells surrounding the volume due to the large gravitational potential at the centre. As discussed in Chapter 3, these cells surround the computational volume and are set to the same density as their neighbour. Mass can therefore be drawn in from these ghost cells given a large enough central potential. To verify this, we did an order of magnitude calculation for the total mass added to the simulation given by,

$$M_{added} = \rho v A t_{grow} \quad (5.2)$$

where ρ is the typical density at the simulation edges, v is the inward velocity at the simulation edges, A is the total surface area over which mass is inflowing, and t_{grow} is the time over which the growth occurs. Using HD6 as an example, the mass growth is roughly linear and occurs only in the last 750,000 years which results in an added mass of $\sim 6 \times 10^4 M_{\odot}$. Since the simulation started with $5.80 \times 10^4 M_{\odot}$ and doubled in mass by the end, we conclude that this is the cause of the growth in mass. The star formation efficiency is then defined as the total mass in cluster particles divided by the total instantaneous mass in the computational volume.

The star formation efficiency shown in Figure 5.6 shows that radiative feedback suppresses the formation of clusters. At the end of RHD6, there is a total of $1.5 \times 10^4 M_{\odot}$ in clusters compared $3 \times 10^4 M_{\odot}$ at the same time in run HD6. These correspond to a star formation efficiency of 25% in RHD6 and 50% in run HD6, a factor of 2

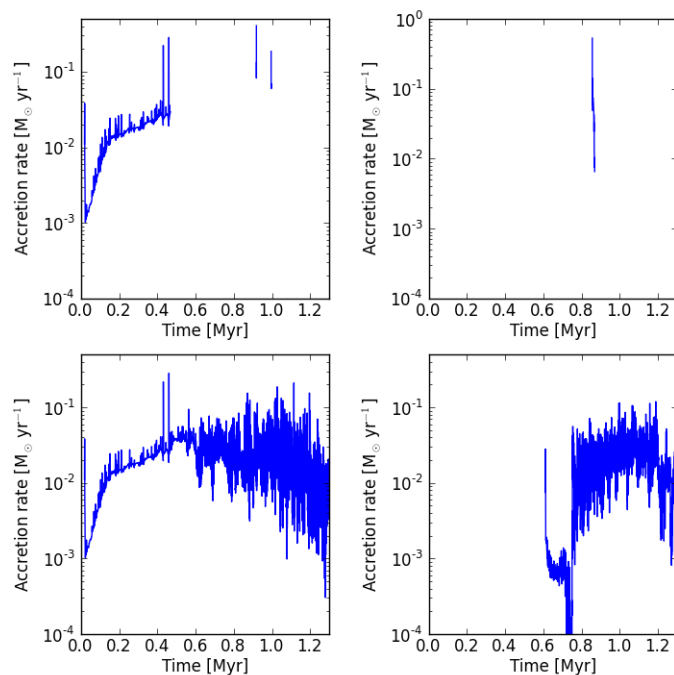


Figure 5.7: The accretion rates as a function of time for the two most massive particles in RHD6 (top) and HD6 (bottom).

difference. This difference in star formation efficiency is consistent with Offner et al. (2009) who also showed radiative feedback decreased the efficiency by a factor of 2.

5.3 Cluster Properties

With a set of full hydrodynamical simulations, we are able to compare the resulting cluster properties to observed clusters and the results from our subgrid modeling described in Chapter 3. The first quantity we have chosen to examine is the accretion rate onto clusters. Unlike the modeling described in Chapter 3, the accretion rate

into our simulated cluster particles is determined by the local environment and not assumed to be constant. In Figure 5.7, we have plotted the cluster particle accretion rates for the two most massive particles in run RHD6 (top row) and HD6 (bottom row). The final masses for the particles shown in Figure 5.7 are 6.97×10^3 and $850 M_{\odot}$ for run RHD6 compared to 5.30×10^4 and $4.43 \times 10^4 M_{\odot}$ in HD6. It can be seen that the accretion rate is not constant with time, as assumed in the modeling, but varies over a few orders of magnitude. The average accretion rate for the particles ranges from 0.002 to $0.03 M_{\odot} \text{ yr}^{-1}$. These average accretion rates fit well within the range assumed in Chapter 3. The large jumps in the accretion rates are due to merging events between cluster particles.

Figure 5.7 also shows the effect of radiative feedback. The particles in run HD6 continue accreting until the end of the simulation. In RHD6 however, the accretion rate drops to zero shortly after the particle's formation. We are again seeing that the heating and dispersal of the gas due to radiative feedback greatly suppresses, and in this case stops altogether, the accretion of mass.

In Figure 5.8, we have plotted the SFR within the three most massive particles in run RHD6. The average SFRs for the cyan, magenta, and yellow tracks are 0.006 , 0.001 , and $0.0005 M_{\odot} \text{ yr}^{-1}$ respectively. Using the final particle masses of 6.97×10^3 , 850 , and $475 M_{\odot}$, we are able to compare the resulting SFRs to the modeling performed in Chapter 3 (see Figure 3.8). The SFRs for regions of the same final mass in Chapter 3 are roughly 0.03 , 0.0004 , and $0.0003 M_{\odot} \text{ yr}^{-1}$. The average SFRs obtained from the simulation clearly are different than those found in the modeling. Moreover, there is no consistent pattern (eg. all higher SFRs in

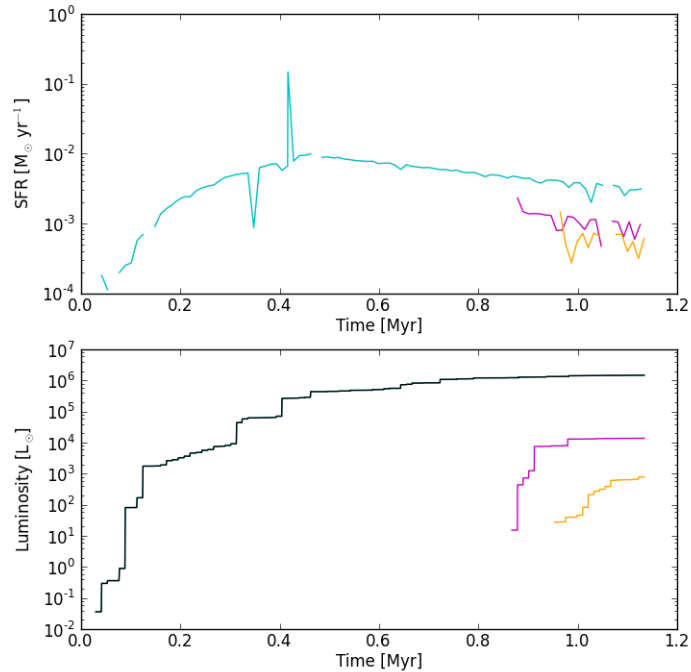


Figure 5.8: **Top:** The SFR as a function of time for the three most massive particles in run RHD6. **Bottom:** The luminosity evolution of the three most massive particles in RHD6 (shown by the dashed lines) and the total luminosity of all particles (solid line). The total luminosity is dominated by one single particle whose track is drawn but cannot be seen because it is covered by the total luminosity line.

the simulation compared to the modeling). This highlights the importance that the accretion history can play in determining the star forming properties of a cluster.

The luminosity of the three most massive particles in RHD6 is shown in the bottom panel of Figure 5.8. The coloured lines represent individual particles while the black line shows the total luminosity of the region. It can be seen that the luminosity is completely dominated by a single particle whose individual luminosity track cannot be seen because it is covered by the solid black line. We are again

able to compare the resulting luminosity to those found in the modeling. The total mass contained in cluster particles at the end of the simulation is $1.80 \times 10^4 M_{\odot}$. From Figure 3.6, a region this massive should have a final luminosity of $\sim 5 \times 10^7 L_{\odot}$, compared to the value of $\sim 2 \times 10^6 L_{\odot}$ that we find in the simulation. This comparison, however, assumes that the total mass in clusters is all contained in a single particle. In our simulations, however, the total mass in clusters is spread across many particles. The amount of gas available for star formation in each particle is therefore less which, as shown in Chapter 3, can prevent the formation of massive stars. If, instead, we compare the luminosity of individual cluster particles to Figure 3.8, we find a much better agreement between the results.

5.4 The subcluster mass function

While we have been defining our particles as distinct clusters, the large grouping of cluster particles at the centre of simulation volume would likely be considered as a single cluster by an observer. We therefore interpret our particles as subclustered regions which, given enough time, will merge to form one large cluster. We will therefore refer to the resulting particle mass distribution as the subcluster mass function (SCMF).

There is observational evidence for subclustering present in the early stages of cluster formation for a variety of star forming regions (Testi et al., 2000; Yan et al., 2010; Gouliermis et al., 2012). These all show that clusters are not born as large, centrally condensed objects but are instead built up of smaller clustered regions

whose stellar densities are significantly higher than the average. The ages of these subclusters are not necessarily the same and can differ by a million years or more. It is estimated that these regions will merge through dynamical interactions in approximately three million years.

There is evidence from our simulation which suggests that our cluster particles represent subclusters of one object rather than many distinct and independent clusters. As can be seen in Figure 5.6, a significant amount of merging has already occurred by 1 Myr which is indicative of subclusters. There is also a significant age spread among the cluster particles. An age spread suggests that each particle is a distinct star forming region which is undergoing collapse independently. This, combined with the fact that the particles are all grouped together within the inner parsec of the simulation volume, suggest we are forming subclusters. Since typical clusters have half mass radii of 0.1-1 pc (Lada & Lada, 2003), there would likely be overlap among the 'clusters'. Therefore, our particles more accurately represent the centers of subclusters.

Unfortunately, there are no measurements of a subcluster mass function with which to compare our resulting mass distribution. This is due to the difficulty involved in defining what constitutes a subcluster. Instead, observational studies tend to focus on single cluster forming regions and attempt to identify whether subclustering is present or not. The focus is therefore not on the properties of subclusters but whether they are present at all. We can, however, still note general properties of the SCMF shown in Figure 5.9.

We find that the largest mass particles form first. This is also seen in run HD6 but the distribution is not shown here due to the low number of cluster particles formed. This is likely due to their location at the centre of the computational volume where there is the largest amount of gas available for fragmentation and further accretion. The burst of particles that forms at ~ 1 Myr fills out the lower mass end of the SCMF.

The final distribution peaks at approximately $50 M_{\odot}$ and has a power law slope of -14. This steep slope suggests that particles are born with a characteristic mass and can fill out the higher mass tail of the SCMF. Since a large number of particles formed close to the end of the simulation, the particles around $50 M_{\odot}$ have not had time to accrete significant mass. Over time the hierarchical merging of subclusters will result in a flattening of the SCMF as objects are moved towards the high mass end of the distribution.

An important note to make is that our particle mass distribution is sensitive to the threshold density required for particle formation. We have chosen a density of 10^4 cm^{-3} to be consistent with observations of star forming clumps (Lada & Lada, 2003). This threshold density corresponds to a Jeans mass of roughly $3.5 M_{\odot}$. By decreasing the threshold density we can increase the Jeans mass which can significantly alter the initial masses of cluster particles. Due to time constraints, the effect of changing the threshold density will not be examined in this work. However, the currently adopted value is consistent with observations and is appropriate for a first attempt.

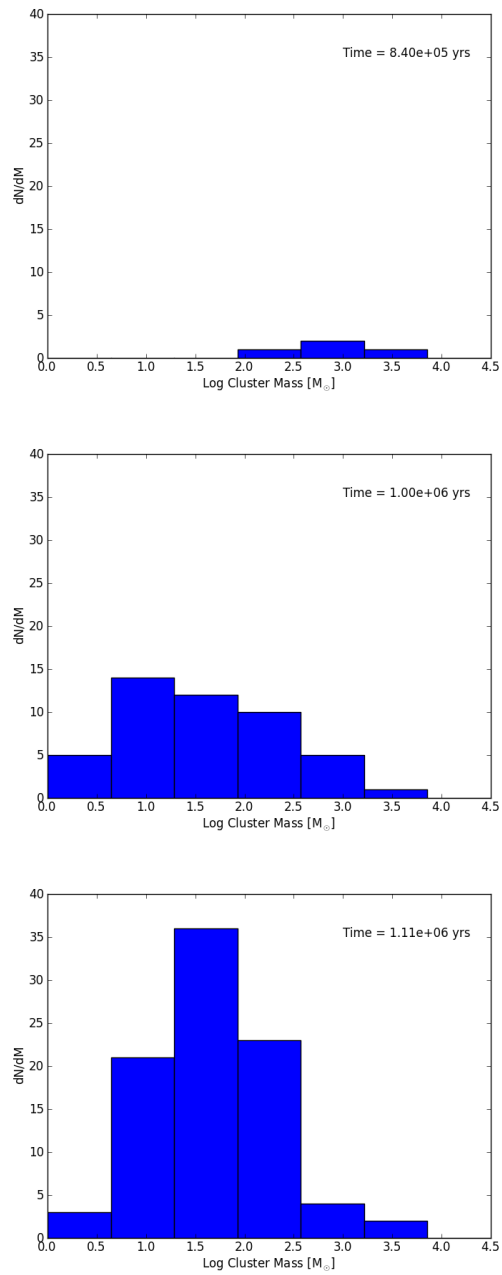


Figure 5.9: The ECMF for run RHD6 shown at three different times. The largest mass particles form first followed by the burst of smaller mass particles which fill out the lower mass end of the ECMF.

While the mass function presented here is for subclusters, we can still compare our distribution to the embedded cluster mass function (ECMF) and note any similarities. From Lada & Lada (2003), the ECMF has a power law slope of -2 which is significantly more shallow than the SCMF. This is not surprising. Since we are looking at the distribution of subcluster masses, we expect a higher number of low mass objects. The ECMF, however, also peaks at $\sim 50 M_{\odot}$. This peak may therefore represent a characteristic cluster mass scale below which there is little star formation activity. It can be argued that the same characteristic peak should be present in both the ECMF and the SCMF. The peak value may represent the typical mass scale for fragmentation out of a dense clump. This could be partly due to the decay of supersonic turbulence which may dissipate on scales corresponding to the peak value. Objects of this mass will therefore be most prevalent in the early phases of cluster formation before significant amounts of merging and dynamical evolution occur (as in the SCMF). However, merging can only occur in regions which have enough mass to form multiple subclusters. Since the ECMF is a census of embedded clusters forming in different regions across the galaxy, there are certainly low mass regions contained in the embedded cluster sample where there may be insufficient mass to form multiple subclustered regions. This would result in the same characteristic scale being reflected in the ECMF. We can therefore view these $\sim 50 M_{\odot}$ as 'cluster seeds', some of which will be able to grow and merge with other subclusters but the majority are unable to do so.

There are a few ways to make a better comparison to the observed ECMF. If the simulation is evolved further, merging between particles may lower the peak of

the SCMF and subsequently raise the high mass tail resulting in a more shallow powerlaw distribution. We could also define an embedded cluster as the total mass in cluster particles contained within a chosen radius. Both these methods could produce SCMF's which better reproduce the observed result but also decrease the total number of clusters leading to a less statistically significant sample. As an alternative, a suite of simulations could be run which vary the initial mass. This would lead to a larger sample size drawn from different star forming environments. This better reflects how the measurements of the ECMF were made; by taking a census of embedded clusters forming in drastically different environments.

Chapter 6

Conclusions

We have shown through the development and implementation of a subgrid model to represent the radiative output of star clusters that radiative feedback can significantly alter the formation and properties of star clusters. This work was divided into two main sections, one which describes and justifies the subgrid model, and one which describes the results of full hydrodynamical simulations which use this model.

The subgrid model used to represent the radiative output of a cluster involves randomly sampling the Chabrier IMF every tenth of freefall which, assuming a density threshold for cluster formation of 10^4 cm^{-3} , amounts to every 36 kyrs. Every time the IMF is sampled, 20% of the available gas inside the cluster is converted to stars whose masses are recorded. The total radiative output of the cluster is then the sum over the outputs of the constituent stars.

To examine the behaviour of our model, a suite of tests was run which varied the initial mass and the accretion rate into the cluster forming clump. The initial masses range between 0 and $10^5 M_{\odot}$ while the accretion rates range from 10^{-5} to $10^{-2} M_{\odot} \text{ yr}^{-1}$. We find that our model can accurately reproduce the ionizing photon

output as compared to more detailed stellar evolution modeling with a clump of mass $10^4 M_{\odot}$ having an ionizing luminosity of $10^{50-51} \text{ s}^{-1}$. Our model also forms the expected number of O stars. Since O stars dominate the luminosity of the cluster, this is a significant result. We have identified a final clump mass threshold for O star formation of $\sim 5000 M_{\odot}$ which is consistent with observations of the ONC.

We have also shown that how a clump gets its mass can affect its star formation properties. The 'reservoir dominated' is characterized by a decreasing SFR while the 'accretion dominated' has an increasing SFR. We find that small ($\sim 100 M_{\odot}$) clusters have SFRs of $10^{-5}-10^{-4} M_{\odot} \text{ yr}^{-1}$ while larger clusters ($> 10^4 M_{\odot}$) can exceed $10^{-2} M_{\odot} \text{ yr}^{-1}$. Lower mass clusters also exhibit more variability in their SFRs than higher mass clusters.

The SFR in a clump is found to scale linearly with the total mass of the cluster. This is consistent with both galactic and extragalactic star forming regions. A timescale for star formation of roughly 3 Myrs has been identified which provides a useful prediction for the expected age range within a young, relatively massive star cluster.

The implementation of our subgrid model into the AMR code FLASH clearly shows that radiative feedback has a significant impact on the formation of clusters. The build up of hot gas in the vicinity of evolving clusters results in large scale outflows. The most important result from our simulations is that radiative feedback decreases the efficiency of cluster formation by a factor of 2, from 50% in the case of no radiative transfer to 25% with radiative transfer.

The simulation with radiative feedback produces significantly more clusters, a total of 95 particles after 1.11 Myrs, compared to the case without radiative transfer which only formed 5. The total mass in cluster particles, however, is less when including radiative feedback. We have interpreted this result as increased subclustering which is seen in other simulations which include radiative feedback.

The resulting distribution of cluster masses has the correct turnover at $50 M_{\odot}$ but has a powerlaw tail which is significantly steeper than the observed ECMF. However, our mass distribution is more aptly described as a subcluster mass distribution since the resulting particles are tightly grouped together and would likely be considered a single large cluster by an observer. This can be overcome by allowing the simulation to evolve further which should decrease the total number of particles through merging, and by running more simulations with varying initial mass.

Future simulations will have varying initial conditions which better represent the observed structure of a molecular cloud. The initial density profile used in this work is a first step but is most likely too centrally peaked resulting in one large cluster at the center. This can be compared against simulations which have a flat top density profile or, better yet, molecular clouds which have been extracted from galactic scale simulations and input into FLASH. This is an important step towards a coherent picture of radiative feedback and its effects on star cluster formation.

Bibliography

- Alves, J., Lombardi, M., & Lada, C. J. 2007, *A&A*, 462, L17
- Andersen, M., Zinnecker, H., Moneti, A., McCaughrean, M. J., Brandl, B., Brandner, W., Meylan, G., & Hunter, D. 2009, *ApJ*, 707, 1347
- André, P., Men'shchikov, A., Könyves, V., & Arzoumanian, D. 2011, in *IAU Symposium*, Vol. 270, *Computational Star Formation*, ed. J. Alves, B. G. Elmegreen, J. M. Girart, & V. Trimble, 255–262
- Arzoumanian, D., André, P., Didelon, P., Könyves, V., Schneider, N., Men'shchikov, A., Soubie, T., Zavagno, A., Bontemps, S., di Francesco, J., Griffin, M., Henneemann, M., Hill, T., Kirk, J., Martin, P., Minier, V., Molinari, S., Motte, F., Peretto, N., Pezzuto, S., Spinoglio, L., Ward-Thompson, D., White, G., & Wilson, C. D. 2011a, *A&A*, 529, L6
- . 2011b, *A&A*, 529, L6+
- Ballesteros-Paredes, J., Gazol, A., Kim, J., Klessen, R. S., Jappsen, A.-K., & Tejero, E. 2006, *ApJ*, 637, 384
- Ballesteros-Paredes, J., Klessen, R. S., Mac Low, M.-M., & Vazquez-Semadeni, E. 2007, *Protostars and Planets V*, 63
- Balsara, D., Ward-Thompson, D., & Crutcher, R. M. 2001, *MNRAS*, 327, 715

Banerjee, R. & Pudritz, R. E. 2006, *ApJ*, 641, 949

—. 2007, *ApJ*, 660, 479

Banerjee, R., Pudritz, R. E., & Anderson, D. W. 2006, *MNRAS*, 373, 1091

Banerjee, R., Pudritz, R. E., & Holmes, L. 2004, *MNRAS*, 355, 248

Bate, M. R. 2009, *MNRAS*, 392, 590

—. 2012, *MNRAS*, 419, 3115

Bate, M. R. & Bonnell, I. A. 2005, *MNRAS*, 356, 1201

Bate, M. R., Bonnell, I. A., & Bromm, V. 2003, *MNRAS*, 339, 577

Bate, M. R. & Burkert, A. 1997, *MNRAS*, 288, 1060

Beltran, M. T., Cesaroni, R., Codella, C., Testi, L., Furuya, R. S., & Olmi, L. 2006, *Nature*, 443, 427

Beltran, M. T., Olmi, L., Cesaroni, R., Schisano, E., Elia, D., Molinari, S., Di Giorgio, A. M., Kirk, J. M., Mottram, J. C., Pestalozzi, M., Testi, L., & Thompson, M. A. 2013, *A&A*, 552, A123

Berger, M. J. & Colella, P. 1989, *Journal of Computational Physics*, 82, 64

Bik, A., Lamers, H. J. G. L. M., Bastian, N., Panagia, N., & Romaniello, M. 2003, *A&A*, 397, 473

Boldyrev, S., Nordlund, Å., & Padoan, P. 2002, *Physical Review Letters*, 89, 031102

Bondi, H. 1952, MNRAS, 112, 195

Bonnell, I. A. 2005, in *Astrophysics and Space Science Library*, Vol. 327, *The Initial Mass Function 50 Years Later*, ed. E. Corbelli, F. Palla, & H. Zinnecker, 425

Bonnell, I. A., Clark, P., & Bate, M. R. 2008, MNRAS, 389, 1556

Bressert, E., Bastian, N., Gutermuth, R., Megeath, S. T., Allen, L., Evans, II, N. J., Rebull, L. M., Hatchell, J., Johnstone, D., Bourke, T. L., Cieza, L. A., Harvey, P. M., Merin, B., Ray, T. P., & Tothill, N. F. H. 2010, MNRAS, 409, L54

Carroll, B. W. & Ostlie, D. A. 1996, *An Introduction to Modern Astrophysics*

Ceverino, D. & Klypin, A. 2009, ApJ, 695, 292

Chabrier, G. 2005, in *Astrophysics and Space Science Library*, Vol. 327, *The Initial Mass Function 50 Years Later*, ed. E. Corbelli, F. Palla, & H. Zinnecker, 41

Chabrier, G. 2009, *Structure Formation in Astrophysics* (Cambridge University Press)

Chabrier, G. & Hennebelle, P. 2010, ApJ, 725, L79

Chomiuk, L. & Povich, M. S. 2011, AJ, 142, 197

Churchwell, E. 2002, ARA&A, 40, 27

Clark, P. C. & Klessen, R. S. 2008, *Astronomische Nachrichten*, 329, 960

Clark, P. C., Klessen, R. S., & Bonnell, I. A. 2007, MNRAS, 379, 57

- Clarke, C. 2010, Royal Society of London Philosophical Transactions Series A, 368, 733
- Commerçon, B., Hennebelle, P., Audit, E., Chabrier, G., & Teyssier, R. 2010, A&A, 510, L3+
- Cox, D. P. 1970, PhD thesis, University of California, San Diego.
- Cunningham, A. J., Klein, R. I., Krumholz, M. R., & McKee, C. F. 2011, ApJ, 740, 107
- Dale, J. E. & Bonnell, I. A. 2008, MNRAS, 391, 2
- Dale, J. E., Bonnell, I. A., Clarke, C. J., & Bate, M. R. 2005, MNRAS, 358, 291
- Dale, J. E., Clark, P. C., & Bonnell, I. A. 2007, MNRAS, 377, 535
- Dale, J. E., Ercolano, B., & Bonnell, I. A. 2012, MNRAS, 424, 377
- Dalgarno, A. & McCray, R. A. 1972, ARA&A, 10, 375
- de Grijs, R. 2010, Royal Society of London Philosophical Transactions Series A, 368, 693
- Dirienzo, W. J., Indebetouw, R., Brogan, C., Cyganowski, C. J., Churchwell, E., & Friesen, R. K. 2012, AJ, 144, 173
- Dubey, A., Fisher, R., Graziani, C., Jordan, IV, G. C., Lamb, D. Q., Reid, L. B., Rich, P., Sheeler, D., Townsley, D., & Weide, K. 2008, in Astronomical Society of the Pacific Conference Series, Vol. 385, Numerical Modeling of Space Plasma Flows, ed. N. V. Pogorelov, E. Audit, & G. P. Zank, 145–+

Duffin, D. F. & Pudritz, R. E. 2008, MNRAS, 391, 1659

Enoch, M. L., Evans, II, N. J., Sargent, A. I., Glenn, J., Rosolowsky, E., & Myers, P. 2008, ApJ, 684, 1240

Faimali, A., Thompson, M. A., Hindson, L., Urquhart, J. S., Pestalozzi, M., Carey, S., Shenoy, S., Veneziani, M., Molinari, S., & Clark, J. S. 2012, MNRAS, 426, 402

Fall, S. M., Krumholz, M. R., & Matzner, C. D. 2010, ApJ, 710, L142

Fall, S. M. & Zhang, Q. 2001, ApJ, 561, 751

Federrath, C., Banerjee, R., Clark, P. C., & Klessen, R. S. 2010, ApJ, 713, 269

Fryxell, B., Olson, K., Ricker, P., Timmes, F. X., Zingale, M., Lamb, D. Q., MacNeice, P., Rosner, R., Truran, J. W., & Tufo, H. 2000, ApJS, 131, 273

Fukui, Y. & Kawamura, A. 2010, ARA&A, 48, 547

Fuller, G. A., Williams, S. J., & Sridharan, T. K. 2005, A&A, 442, 949

Gao, Y. & Solomon, P. M. 2004, ApJ, 606, 271

Goodwin, S. P., Nutter, D., Kroupa, P., Ward-Thompson, D., & Whitworth, A. P. 2008, A&A, 477, 823

Gouliermis, D. A., Schmeja, S., Dolphin, A. E., Gennaro, M., Tognelli, E., & Prada Moroni, P. G. 2012, ApJ, 748, 64

Hansen, C. E., Klein, R. I., McKee, C. F., & Fisher, R. T. 2012, ApJ, 747, 22

Harper-Clark, E. 2011, PhD thesis, University of Toronto (Canada)

Hartmann, L. & Burkert, A. 2007, *ApJ*, 654, 988

Heitsch, F., Mac Low, M.-M., & Klessen, R. S. 2001, *ApJ*, 547, 280

Hennebelle, P. & Fromang, S. 2008, *A&A*, 477, 9

Hensler, G. 2011, in *IAU Symposium*, Vol. 270, *Computational Star Formation*, ed. J. Alves, B. G. Elmegreen, J. M. Girart, & V. Trimble, 309–317

Hill, T., Motte, F., Didelon, P., Bontemps, S., Minier, V., Hennemann, M., Schneider, N., André, P., Men'shchikov, A., Anderson, L. D., Arzoumanian, D., Bernard, J.-P., di Francesco, J., Elia, D., Giannini, T., Griffin, M. J., Kirk, J., Konyves, V., Marston, A. P., Martin, P., Molinari, S., Nguyen Luong, Q., Peretto, N., Pezzuto, S., Roussel, H., Sauvage, M., Soubie, T., Testi, L., Ward-Thompson, D., White, G. J., Wilson, C. D., & Zavagno, A. 2011a, *ArXiv e-prints*: 1108.0941

Hill, T., Motte, F., Didelon, P., Bontemps, S., Minier, V., Hennemann, M., Schneider, N., André, P., Men'shchikov, A., Anderson, L. D., Arzoumanian, D., Bernard, J.-P., di Francesco, J., Elia, D., Giannini, T., Griffin, M. J., Könyves, V., Kirk, J., Marston, A. P., Martin, P. G., Molinari, S., Nguyen Luong, Q., Peretto, N., Pezzuto, S., Roussel, H., Sauvage, M., Soubie, T., Testi, L., Ward-Thompson, D., White, G. J., Wilson, C. D., & Zavagno, A. 2011b, *A&A*, 533, A94

Hillenbrand, L. A. 1997, *AJ*, 113, 1733

Hillenbrand, L. A. & Hartmann, L. W. 1998, *ApJ*, 492, 540

Hopkins, P. F., Quataert, E., & Murray, N. 2012, MNRAS, 421, 3522

Hosokawa, T. & Omukai, K. 2009, ApJ, 703, 1810

Hunter, D. A., O'Neil, Jr., E. J., Lynds, R., Shaya, E. J., Groth, E. J., & Holtzman, J. A. 1996, ApJ, 459, L27

Johnstone, D., Fich, M., Mitchell, G. F., & Moriarty-Schieven, G. 2001, ApJ, 559, 307

Kennicutt, R. C. & Evans, N. J. 2012, ARA&A, 50, 531

Kevlahan, N. & Pudritz, R. E. 2009, ApJ, 702, 39

Kim, J.-h., Krumholz, M. R., Wise, J. H., Turk, M. J., Goldbaum, N. J., & Abel, T. 2012, ArXiv e-prints

Kirk, H., Johnstone, D., & Tafalla, M. 2007, ApJ, 668, 1042

Kirk, H., Myers, P. C., Bourke, T. L., Gutermuth, R. A., Hedden, A., & Wilson, G. W. 2013, ApJ, 766, 115

Klassen, M., Pudritz, R. E., & Peters, T. 2012, MNRAS, 421, 2861

Klessen, R. S. 2001, ApJ, 556, 837

Klessen, R. S., Heitsch, F., & Mac Low, M.-M. 2000, ApJ, 535, 887

- Könyves, V., André, P., Men'shchikov, A., Schneider, N., Arzoumanian, D., Bon-
temps, S., Attard, M., Motte, F., Didelon, P., Maury, A., Abergel, A., Ali, B.,
Baluteau, J.-P., Bernard, J.-P., Cambrésy, L., Cox, P., di Francesco, J., di Gior-
gio, A. M., Griffin, M. J., Hargrave, P., Huang, M., Kirk, J., Li, J. Z., Martin, P.,
Minier, V., Molinari, S., Olofsson, G., Pezzuto, S., Russeil, D., Roussel, H., Sara-
ceno, P., Sauvage, M., Sibthorpe, B., Spinoglio, L., Testi, L., Ward-Thompson, D.,
White, G., Wilson, C. D., Woodcraft, A., & Zavagno, A. 2010, *A&A*, 518, L106
- Kroupa, P., Weidner, C., Pflamm-Altenburg, J., Thies, I., Dabringhausen, J., Marks,
M., & Maschberger, T. 2013, *The Stellar and Sub-Stellar Initial Mass Function of
Simple and Composite Populations*, ed. T. D. Oswalt & G. Gilmore, 115
- Krumholz, M. R., Cunningham, A. J., Klein, R. I., & McKee, C. F. 2010, *ApJ*, 713,
1120
- Krumholz, M. R., Klein, R. I., & McKee, C. F. 2011, *ApJ*, 740, 74
- Krumholz, M. R., McKee, C. F., & Klein, R. I. 2005, *ArXiv Astrophysics e-prints*
- . 2006a, *ApJ*, 638, 369
- . 2006b, *ApJ*, 638, 369
- . 2006c, *ApJ*, 638, 369
- Krumholz, M. R. & Thompson, T. A. 2012, *ApJ*, 760, 155
- Kuiper, R., Klahr, H., Beuther, H., & Henning, T. 2010, *ApJ*, 722, 1556
- . 2012, *ArXiv e-prints*

Lada, C. J. 2010, Royal Society of London Philosophical Transactions Series A, 368, 713

Lada, C. J. & Lada, E. A. 2003, ARA&A, 41, 57

Lada, C. J., Lombardi, M., & Alves, J. F. 2010a, ApJ, 724, 687

—. 2010b, ApJ, 724, 687

Levermore, C. D. & Pomraning, G. C. 1981, ApJ, 248, 321

Li, Z.-Y. & Nakamura, F. 2006, ApJ, 640, L187

Massey, P. & Hunter, D. A. 1998, ApJ, 493, 180

Matzner, C. D. & McKee, C. F. 2000, ApJ, 545, 364

Maury, A. J., André, P., & Li, Z.-Y. 2009, A&A, 499, 175

McKee, C. F. & Ostriker, E. C. 2007, ARA&A, 45, 565

McKee, C. F. & Tan, J. C. 2003a, ApJ, 585, 850

—. 2003b, ApJ, 585, 850

Megeath, S. T., Gutermuth, R., Muzerolle, J., Kryukova, E., Flaherty, K., Hora, J. L., Allen, L. E., Hartmann, L., Myers, P. C., Pipher, J. L., Stauffer, J., Young, E. T., & Fazio, G. G. 2012, AJ, 144, 192

Melena, N. W., Massey, P., Morrell, N. I., & Zangari, A. M. 2008, AJ, 135, 878

Mellon, R. R. & Li, Z.-Y. 2008, ApJ, 681, 1356

Mezger, P. G. & Henderson, A. P. 1967, *ApJ*, 147, 471

Minerbo, G. N. 1978, *J. Quant. Spec. Radiat. Transf.*, 20, 541

Motte, F., André, P., Ward-Thompson, D., & Bontemps, S. 2001, *A&A*, 372, L41

Murray, N. & Chang, P. 2012, *ApJ*, 746, 75

Murray, N., Quataert, E., & Thompson, T. A. 2010, *ApJ*, 709, 191

Myers, P. C. & Goodman, A. A. 1988, *ApJ*, 326, L27

Nordlund, Å. 2011, in *IAU Symposium, Vol. 270, Computational Star Formation*,
ed. J. Alves, B. G. Elmegreen, J. M. Girart, & V. Trimble, 207–214

Nutter, D. & Ward-Thompson, D. 2007, *MNRAS*, 374, 1413

Offner, S. S. R., Klein, R. I., McKee, C. F., & Krumholz, M. R. 2009, *ApJ*, 703, 131

Offner, S. S. R. & McKee, C. F. 2011, *ApJ*, 736, 53

Osterbrock, D. E. 1989, *Astrophysics of gaseous nebulae and active galactic nuclei*,
ed. Osterbrock, D. E.

Padoan, P. & Nordlund, Å. 2002a, *ApJ*, 576, 870

—. 2002b, *ApJ*, 576, 870

Padoan, P. & Nordlund, Å. 2005, in *Astrophysics and Space Science Library, Vol. 327*,
The Initial Mass Function 50 Years Later, ed. E. Corbelli, F. Palla, & H. Zinnecker,
357

Pang, X., Grebel, E. K., Allison, R. J., Goodwin, S. P., Altmann, M., Harbeck, D., Moffat, A. F. J., & Drissen, L. 2013, *ApJ*, 764, 73

Parker, R. J. & Dale, J. E. 2013, *MNRAS*, 432, 986

Peters, T., Banerjee, R., Klessen, R. S., Mac Low, M.-M., Galván-Madrid, R., & Keto, E. R. 2010, *ApJ*, 711, 1017

Peters, T., Schleicher, D. R. G., Klessen, R. S., Banerjee, R., Federrath, C., Smith, R. J., & Sur, S. 2012, *ApJ*, 760, L28

Price, D. J. & Bate, M. R. 2009, *MNRAS*, 398, 33

Pudritz, R. E. 2002, *Science*, 295, 68

Pudritz, R. E. & Kevlahan, N. K.-R. 2012, *ArXiv e-prints*

Pudritz, R. E., Ouyed, R., Fendt, C., & Brandenburg, A. 2007, *Protostars and Planets V*, 277

Rathborne, J. M., Lada, C. J., Muench, A. A., Alves, J. F., Kainulainen, J., & Lombardi, M. 2009, *ApJ*, 699, 742

Ricker, P. M., Calder, A. C., Dursi, L. J., Fryxell, B., Lamb, D. Q., MacNeice, P., Olson, K., Rosner, R., Timmes, F. X., Truran, J. W., Tufo, H. M., & Zingale, M. 2001, in *American Institute of Physics Conference Series*, Vol. 583, American Institute of Physics Conference Series, 316–318

Rijkhorst, E.-J., Plewa, T., Dubey, A., & Mellema, G. 2006, *A&A*, 452, 907

Salpeter, E. E. 1955, *ApJ*, 121, 161

Schmeja, S. & Klessen, R. S. 2004, *A&A*, 419, 405

Schneider, N., Csengeri, T., Hennemann, M., Motte, F., Didelon, P., Federrath, C., Bontemps, S., Di Francesco, J., Arzoumanian, D., Minier, V., André, P., Hill, T., Zavagno, A., Nguyen-Luong, Q., Attard, M., Bernard, J.-P., Elia, D., Fallscheer, C., Griffin, M., Kirk, J., Klessen, R., Könyves, V., Martin, P., Men'shchikov, A., Palmeirim, P., Peretto, N., Pestalozzi, M., Russeil, D., Sadavoy, S., Soubie, T., Testi, L., Tremblin, P., Ward-Thompson, D., & White, G. 2012, *A&A*, 540, L11

Seifried, D., Banerjee, R., Pudritz, R. E., & Klessen, R. S. 2013, *ArXiv e-prints*

Shields, G. A. 1990, *ARA&A*, 28, 525

Smith, L. J., Norris, R. P. F., & Crowther, P. A. 2002, *MNRAS*, 337, 1309

Sternberg, A., Hoffmann, T. L., & Pauldrach, A. W. A. 2003, *ApJ*, 599, 1333

Tasker, E. J. 2011, *ApJ*, 730, 11

Teixeira, P. S., Lada, C. J., Young, E. T., Marengo, M., Muench, A., Muzerolle, J., Siegler, N., Rieke, G., Hartmann, L., Megeath, S. T., & Fazio, G. 2006, *ApJ*, 636, L45

Testi, L., Sargent, A. I., Olmi, L., & Onello, J. S. 2000, *ApJ*, 540, L53

Throop, H. B. & Bally, J. 2008, *AJ*, 135, 2380

Tout, C. A., Pols, O. R., Eggleton, P. P., & Han, Z. 1996, *MNRAS*, 281, 257

Truelove, J. K., Klein, R. I., McKee, C. F., Holliman, II, J. H., Howell, L. H., & Greenough, J. A. 1997, ApJ, 489, L179+

Vázquez-Semadeni, E., Gazol, A., & Scalo, J. 2000, ApJ, 540, 271

Vázquez-Semadeni, E., Ryu, D., Passot, T., González, R. F., & Gazol, A. 2006, ApJ, 643, 245

Veltchev, T. V., Donkov, S., & Klessen, R. S. 2013, MNRAS, 432, 3495

Whitehouse, S. C., Bate, M. R., & Monaghan, J. J. 2005, MNRAS, 364, 1367

Williams, J. P. & McKee, C. F. 1997, ApJ, 476, 166

Wu, J., Evans, II, N. J., Gao, Y., Solomon, P. M., Shirley, Y. L., & Vanden Bout, P. A. 2005, ApJ, 635, L173

Yan, C.-H., Minh, Y. C., Wang, S.-Y., Su, Y.-N., & Ginsburg, A. 2010, ApJ, 720, 1

Zavagno, A., Russeil, D., Motte, F., Anderson, L. D., Deharveng, L., Rodón, J. A., Bontemps, S., Abergel, A., Baluteau, J.-P., Sauvage, M., André, P., Hill, T., & White, G. J. 2010, A&A, 518, L81